POLITECNICO DI TORINO

Corso di Laurea in Ingegneria Aerospaziale

TESI DI LAUREA MAGISTRALE

Design of a Test Bench for the Development and Validation of Prognostic Algorithms for Electromechanical Actuators

Relatori

Prof. Paolo Maggiore

Ing. Matteo Davide Lorenzo Dalla Vedova

Ing. Pier Carlo Berri

Candidato

MattiaTedde

Luglio 2020

Contents

Index of Figures

Index of Tables

Introduction

In this thesis is presented the study and the process of development of a test bench with the aim of simulating the actuation process of an on-board electromechanical actuation system.

This study was mainly carried out with a “system design” approach focusing on acquiring and fitting together all the different components to define and realize the overall architecture of the test bench. Some components like the braking mechanism and other small supports required a complete internal design that was carried out starting from rough sketches, to 3D models and then the detailed 2D drawings so that they could be crafted by an external dedicated company. The reduction gear was completely designed and manufactured internally by the Politecnico di Torino with the use of Fused Deposition Modelling (FDM) additive manufacturing. The planetary reduction gearbox was realized as part of a previous study but already carried out with the aim of introducing it later in a test bench intended for Electromechanical Actuators (EMAs) tests.

The test bench under development replicates the architecture of a typical secondary flight control elecromechanical actuator. The same standard actuators that can be found onboard on standard aircrafts for the actuation of high lift devices like slats. The system architecture was also provided with a braking system able to load the electric motor with a desired braking torque. This load is going to simulate an external force like the aerodynamic load on the flight control surface while it is being actuated.

This study is going to settle the foundation for the later development and validation of prognostic algorithms for EMAs which requires an extensive set of data about operating parameters. This kind of data, generally not easily available, is going to be produced by the test bench which is going to be able to function in several different operating scenarios to simulate conditions both nominal and under the effect of faults.

1 | Flight Control System

Aircraft flight controls are the means by which a pilot controls the direction and attitude of an aircraft. Their purpose is to modify the airflow and pressure distribution around the airfoil in order to change the aircraft attitude and trajectory during flight. An aircraft flight control system consists of primary and secondary systems.

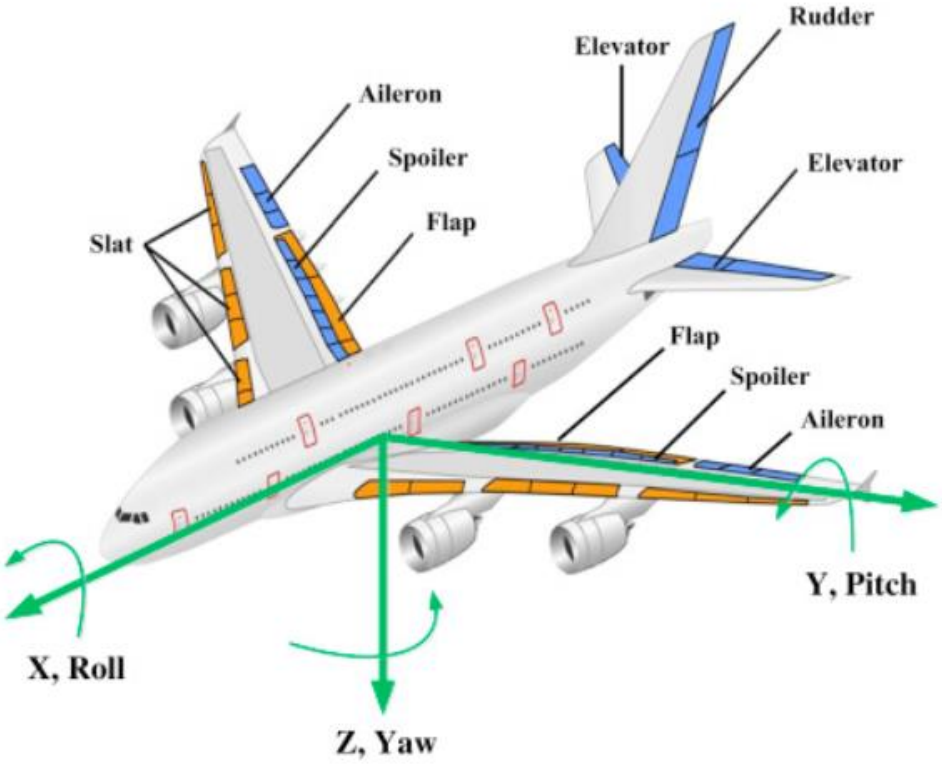

Figure 1: standard flight controls on a commercial aircraft

1.1 Primary Flight Controls

The ailerons, elevator (or stabilator), and rudder constitute the primary flight control system and are required to control an aircraft safely during flight.

Movement of any of the three primary flight control surfaces causes unbalanced aerodynamic torques which are used to move the aircraft about its three axes. These changes affect the lift and drag produced by the airfoil/ control surface combination and allow the pilot to control the aircraft.

All sort of disturbances may occur during the flight period and that is why the primary flight controls must be always active and able to correct or change the flight path; to do so they must be instinctive and have a high cutoff frequency.

Aircraft control systems are designed to provide proportional forces with respect to the ones acting on the airframe. At low airspeed, the controls usually fell soft, and the aircraft responds slowly to the pilot applications on the controls. At higher airspeed, the controls become progressively stiff and the aircraft response is quicker.

Primary flight controls are essential to the accomplishment of any flight mission and the loss of it can result in a catastrophic failure for the aircraft. That is why the reliability requirements for this system are very high and multiple redundancies are needed beside a backup operating mode.

As said before the standard primary flight control surfaces used on most aircraft are the following:

- Ailerons: mounted on the trailing edge of each wing near the wingtips and able move in opposite directions. Their function is to achieve rolling moments about the x body axis
- Elevator: is located on the horizontal stabilizer and its movement can cause a pitching moment about the y body axis
- Rudder: typically positioned on the trailing edge of the vertical empennage and able to generate a yawing moment about the y body axis

The ones mentioned above are not the only solutions that can be adopted. In military aircrafts for example unconventional solutions for control surfaces may be adopted:

- Canards: used for pitch control and consist of a small forewing placed forward of the main wing
- Elevons: which are moving surfaces that combine the functions of the elevator and ailerons often used on tailless aircrafts
- V-tails: two surfaces set in a V-shaped configuration which combine the function of both rudder and elevator and generate control moments about more than one axis

Depending on how fast or heavy the aircraft can be the pilot might not be able to self-compensate the surface hinge moment with an adequate control force despite using aerodynamic compensation. That is why primary flight controls can be either powered or reversible:

- Powered: due to the growth of friction and inertia of the actuation system a hydraulic of electric system provide the required mechanical power required to actuate the control surfaces. The pilot must only provide the input signal. This kind of flight control requires artificial fell devices that allow tactile feedback of airspeed to the pilot which otherwise would be isolated from the aerodynamic feedback forces.
- Reversible: this kind of flight control is more primitive and is used on small aircraft where the aerodynamic forces are relatively low and can be easily compensated by the pilot. Reversible flight controls directly link the pilot, which operates with pedals or a stick, to the surfaces by a mechanical system made of steel cables and/or rods.

1.2 Secondary Flight Controls

Secondary flight controls include all those devices designed to manage the aerodynamic coefficients in order to better perform in different flight conditions.

The standard secondary flight controls are:

- Flaps: high-lift devices attached to the trailing edge of the wing, their function is to increase both lift and induced drag from any angle of attack.

- Slats: placed on the wing's leading edge they are intended to let the air below the wing to flow over the wing 's upper surface, delaying the air separation and preventing stall at high angle of attack.
- Spoilers and Speedbrakes: located on the wing upper surface, their role is to interrupt the steady airflow over the wing, reducing lift and increasing drag.

Exception made for the spoilers, which can be actuated asymmetrically to better perform roll manoeuvres, all secondary control surfaces are actuated by a mechanical power train that ensure a symmetrical actuation of the desired control. Unlike primary flight controls these surfaces are only necessary in specific phases of a flight mission and that is why a high frequency response is unnecessary and the actuation is made with an ON/OFF switch.

2 | Electro-Mechanical Actuators

Conventional hydraulic actuators in aircraft systems are high maintenance and more vulnerable to high temperatures and pressures. This usually leads to high operating costs and low efficiency. With the rapid development of More/All Electric technology, Electro-Mechanical Actuators (EMA) are being broadly employed to improve the maintainability, reliability, and manoeuvrability of future aircraft.

In recent years, the trend of the aerospace industry is to enhance the use of the electrical actuation system that is commonly called power-by wire actuation (PBW) to achieve a More/All Electric Aircraft (MEA/AEA).

The PBW technology looks for different design approaches and extends the use of electrically powered actuators which can be used in different subsystems such as: flight control, landing gear, engine actuation system and more.

Studies have shown that PBW actuators will benefit the actuation system with many advantages due to their capabilities of being fault-tolerant and able to operate without the use of fluids and pipes. These advantages include:

- Enhanced safety and reliability due to the absence of poisonous and flammable hydraulic fluids
- Reduced weight, volume, and complexity of power transmission paths
- Easier maintenance and less costs due to the lack of hydraulic leaks
- Better diagnostic capability
- Higher energy efficiency and better dynamic characteristics

These kinds of actuators are already onboard and operative on large commercial transport aircrafts. For example, EMA are used for landing gear braking, mid spoiler surfaces, and trimmable horizontal stabilizer on Boeing 787. On Airbus A380, Electro-Hydrostatic Actuators (EHA) are already in service for primary flight controls (ailerons and

elevators), while EMAs are employed for slats, trimmable horizontal stabilizer, and thrust reverser actuation.

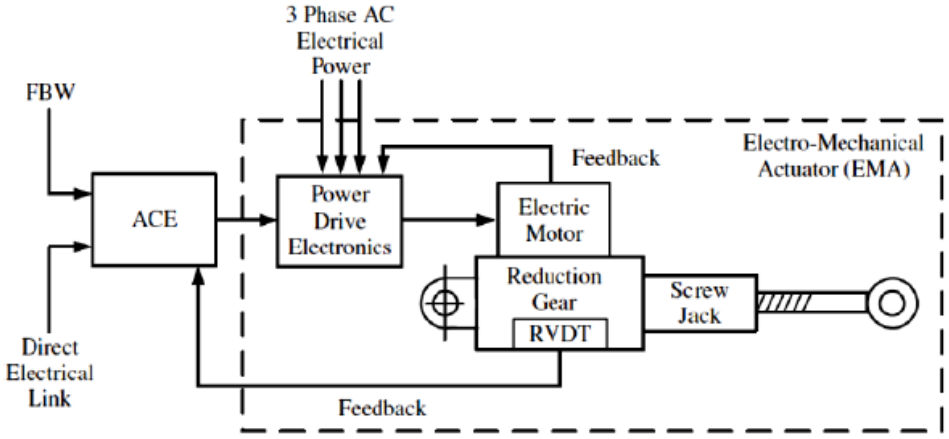

Figure 2: scheme of a standard EMA

As shown in *figure 2* EMAs are usually composed of the following components:

- An Actuator Control Electronics unit which role is to execute a control logic and close the feedback loop by always comparing the command position with the actual position of the utilizer;
- A Power Drive Electronics system used to switch the DC current into a three phase AC current to operate the electric motor;
- An Electric Motor often BLDC which transforms the electric power into mechanical power;
- A Reduction Gear to reduce the motor angular speed (RPM) and raise its torque;
- A mechanism to transform the rotary motion given by the electric motor into linear motion;
- A grid of sensors able to acquire the actual position of the utilizer and feed this signal to the ACE;

EMAs can be divided into two main classes depending on how they transmit the motion on the utilizer:

- Linear EMAs: these kinds of actuators usually utilize a roller or ball screw mechanism in order to transform the rotational motion of the motor into a linear motion. Linear EMAs can be also classified into:
    - ❖ Geared: present a reduction stage connected to the motor;
    - ❖ Direct drive: the motor is directly connected to the screw;
- Rotative EMAs: the rotative motion, usually, after passing through a reduction stage, is directly fed to the utilizer.

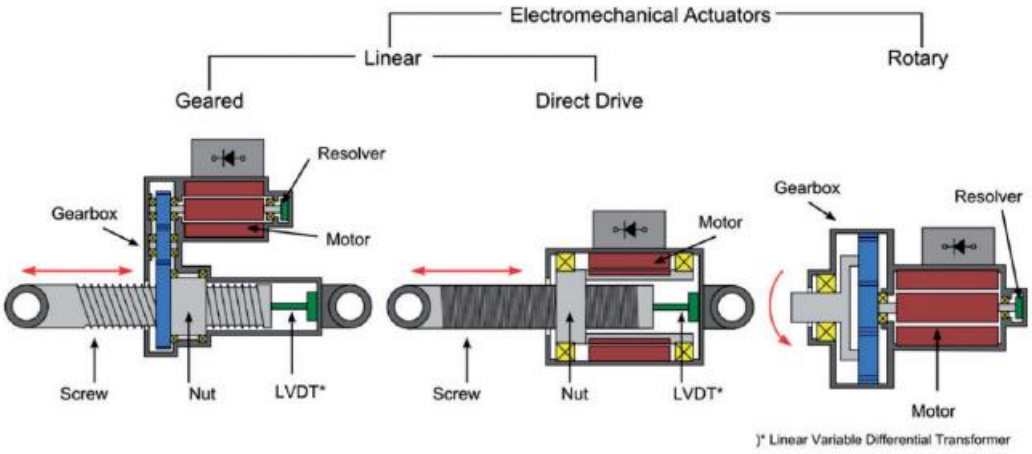

Figure 3: different classes of EMAs [1]

2.1 Brushless Motors

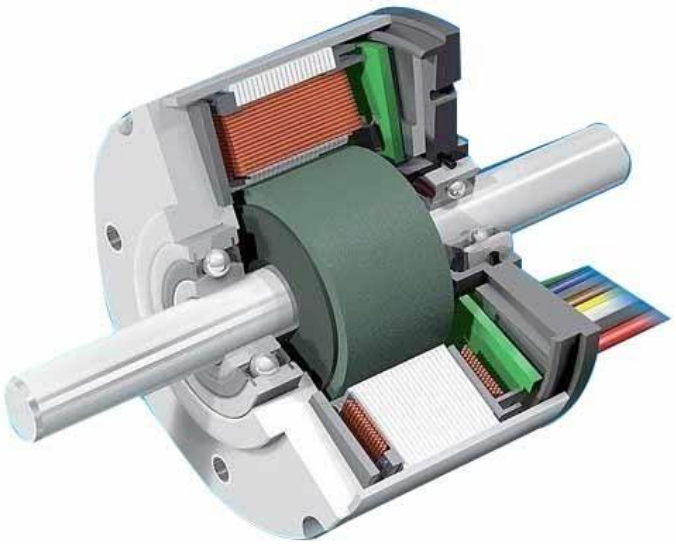

Figure 4: cross view of a brushless motor

The resistance to harsh environments and shocks beside a compact and durable design made the Brushless DC motors (BLDC) ideal for aerospace applications. In fact, they are commonly used in the electromechanical servoactuators needed for flight control. The architecture of BLDC motors is based on a stator in which are placed three star connected phase windings and a permanent magnet rotor. Having the windings positioned on the stator made BLDC perfect for the aerospace industry since this simple change eliminates all the complications associated with brushed DC motors such as the wearing of the brushes which implies constant maintenance, the production of sparkles which made them impractical in certain kind of environments and a major electromagnetic noise. Due to the absence of a brush commutator to properly function the BLDC motor needs an electronic controller to power the three electric phases accordingly to the rotor angular position. The rotor exact angular position is given by specific sensors. The most typical design features Hall effect sensors which can sense the magnetic field produced by the permanent magnet and therefore determine the rotor position. Other controllers can instead feature a back-EMF measurement in the undriven coils to determine the rotor position, eliminating the need for Hall effect sensors, they are indeed called sensorless controllers. Sensors based

on counter electromotive force can be cheaper and an easier solution for a controller design but they can face some difficulties in the measurement of back-EMF at low angular velocities ,typical of aeronautical servoactuators, and therefore they are only suitable to open loop applications.

2.1.1 Stator

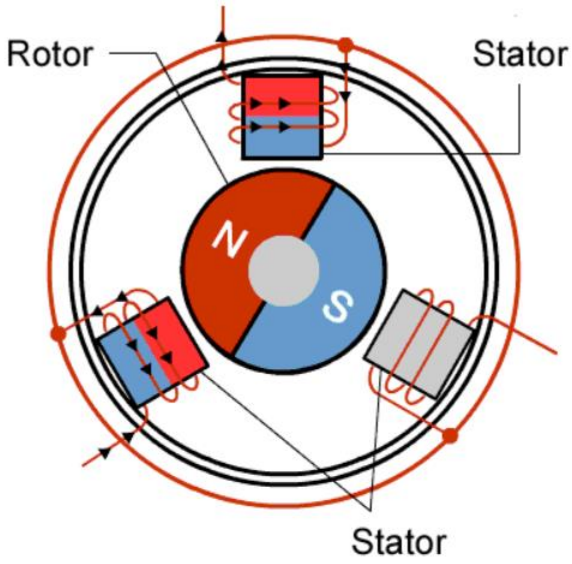

Figure 5: simplified view of the main parts of a brushless motor

In a BLDC motor the stator is made up of a laminated steel stacked so it can carry the windings. The windings can be designed in two different patterns: a delta pattern(Δ) or star pattern (Y). The leading divergence between the two configurations is that the Y pattern gives high torque at low RPM while the Δ pattern gives low torque at low RPM. This as a result of the fact that in the Δ arrangement half of the voltage is applied to the undriven winding, therefore the losses are increased and as a result also efficiency and torque. Steel lamination in the stator can be either slotted or slotless. Slotless motors are more versatile since they can work effectively both at very high and low angular speeds. Very high speeds can be reached thanks to a lower inductance while the low ones are achievable thanks to the absence of teeth in the lamination stack which reduce the cogging torque making the rotation smooth even at low speeds. The main disadvantage of slotless motors is a higher cost due to the requirements of more winding to compensate the larger air gap.

2.1.2 Rotor

The rotor of a common BLDC motor is made out permanent magnets. The material chosen to build the permanent magnets can vary depending on the requirements since a material with a higher flux density can make the motor achieve a higher torque. The most commonly used material is Neodymium-Iron-Boron alloy.

The number of poles in a rotor can vary. Depending on the application, having a higher number of poles can be better to achieve a smoother torque delivery but keeping in mind that the maximum speed is going to be lower due to limitation on the maximum commutation frequency of power transistors in the controller.

As shown in *figure 6*, depending on both the shape and the placement, the rotor structure can assume two different configurations from a magnetic point of view. The isotropic configuration features permanent magnets located inside the cylindrical body of the rotor while in the anisotropic configuration the magnets are fixed to the outer surface of the body. The magnets during the operating phases are always undergoing high levels of mechanical stress because of the very high angular velocity that the rotor can easily reach (thousands of RPM).

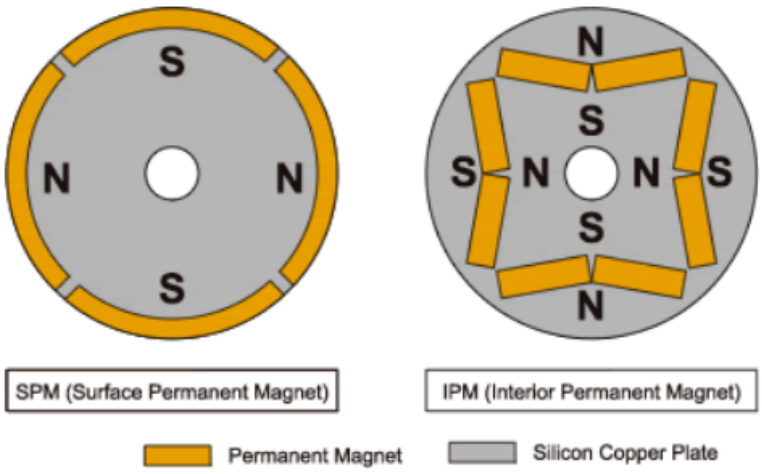

Figure 6: isotropic and anisotropic configuration

2.1.3 Working Principles and Operation

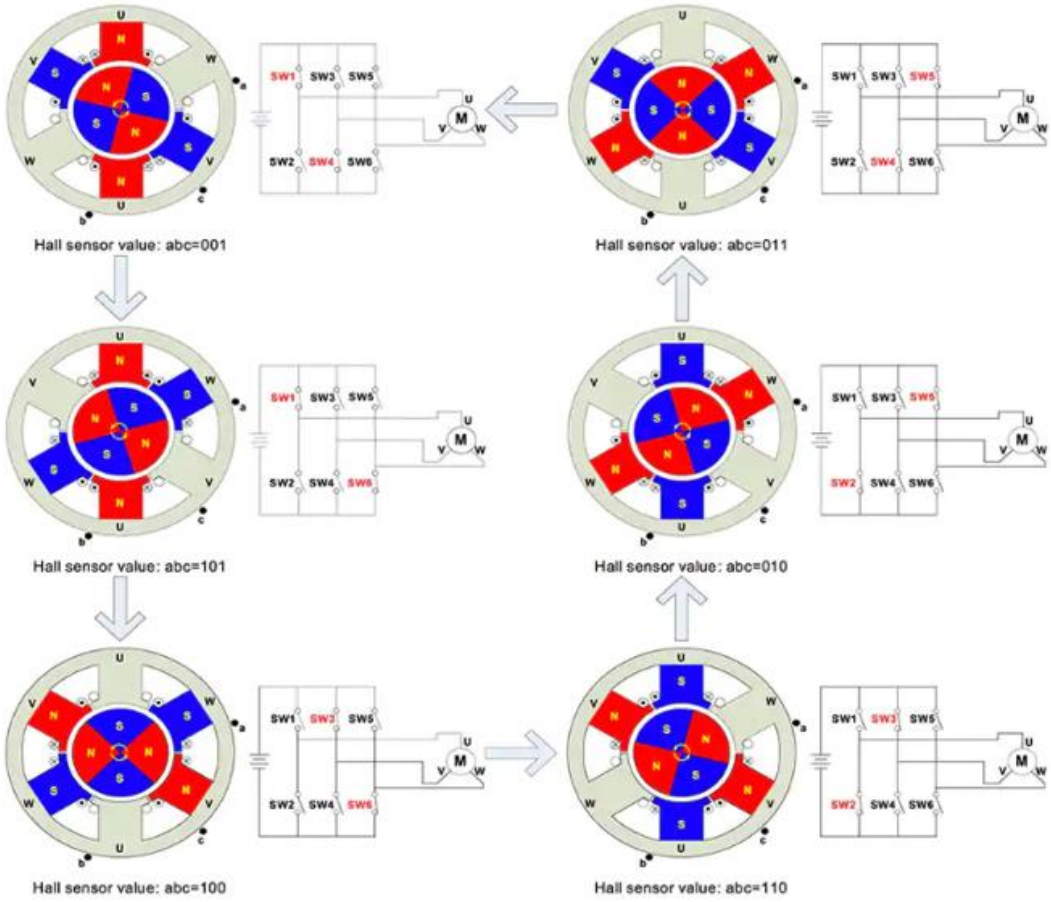

Figure 7: commutation steps of a three phase BLDC motor

The working principles of a BLDC motor are essentially the same of a brushed DC motor: internal shaft position feedback in order to actuate a phase commutation logic. In a common brushed DC motor, the feedback is achieved mechanically by a commutator and the brushes while in a BLDC motor the process is actuated by the Hall sensors that can register the rotor position and send it to a solid state inverter that can operate the commutation. In a common BLDC motor, three Hall sensors can be found placed at 120° one from another on the stator circumference. These sensors can provide a position signal with a 60° accuracy which means that every 60° the magnetic field shifts its polarity and the signal is given to the controller which processes the rotor position and therefore determines which phase is going to be powered.

BLDC motor can be divided in two main groups depending on the commutation techniques and its waveform:

Square wave commutation: takes its name because the phase current waveform is a square wave. Suitable in case not very high performance are required; the commutation

pattern is controlled by a three-phase bridge inverter composed of six switching devices. The advantages a square wave control are the simple control algorithm and a low hardware cost which determine its ease of implementation.

Sine wave commutation: the windings are actuated with a specific voltage so that the phase form of the motor is a sine wave. Every coil is exerted ate the same time with a current having a sinusoidal waveform but each with 120° offset. This particular technique ensures a smoother rotation of the electromagnetic field and therefore a smoother actuation of the rotor during its motion and a better dynamic response. These characteristics make this commutation logic superior to the previous one in terms of performance but more demanding in terms of costs and complexity.

3 | Development of the Testing Bench

The aim of this project is the development of a test bench for EMAs with the future goal of starting to develop and validate prognostic algorithm for this kind of actuators. To simulate at its best the functioning of an onboard EMA, a testing bench and a complete system able to collect all the data needed for the analysis and implementation of the algorithms had to be designed. Some mechanical parts of the testing system are shown in the sketch in *figure 8*. The highlighted block can be divided in two main modules connected to each other by a transmission chain.

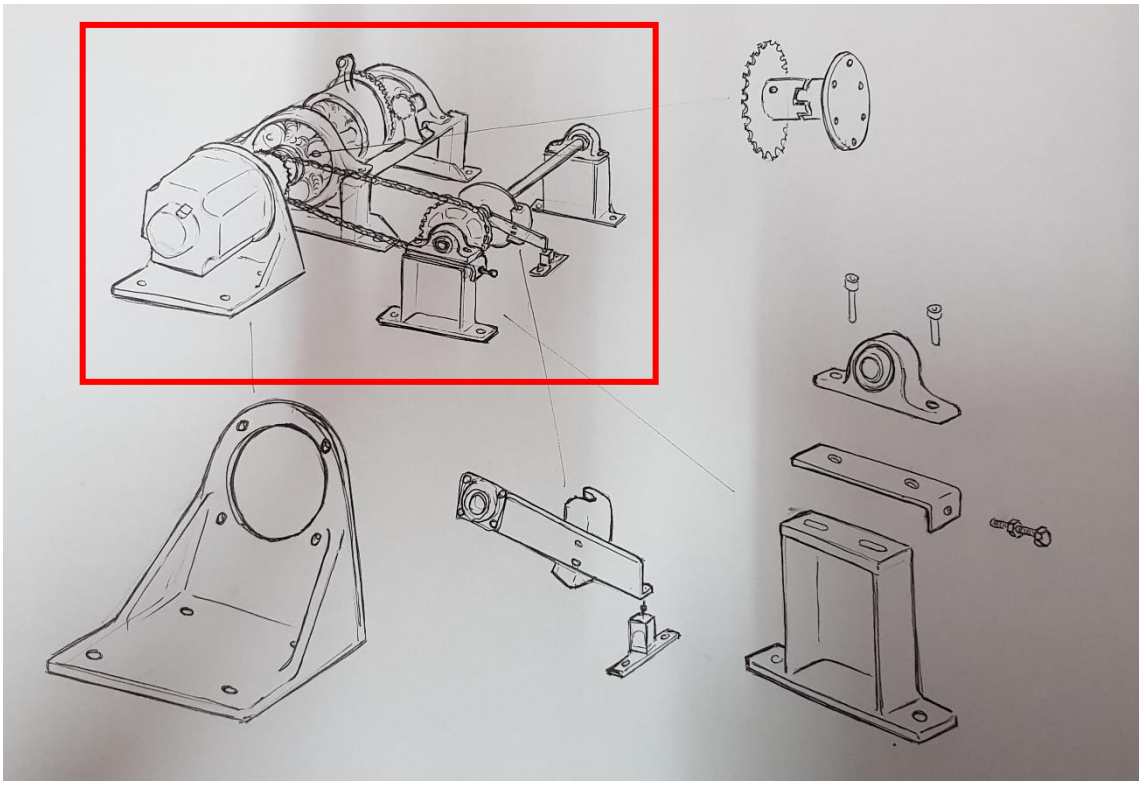

Figure 8: first sketch of the main mechanical components of the test bench

The module on the left is going to be called “actuation module” while the one on the right is the “braking module” which is designed to simulate a load on the motor shaft.

In *figure 9* is shown a simplified scheme of the entire system.

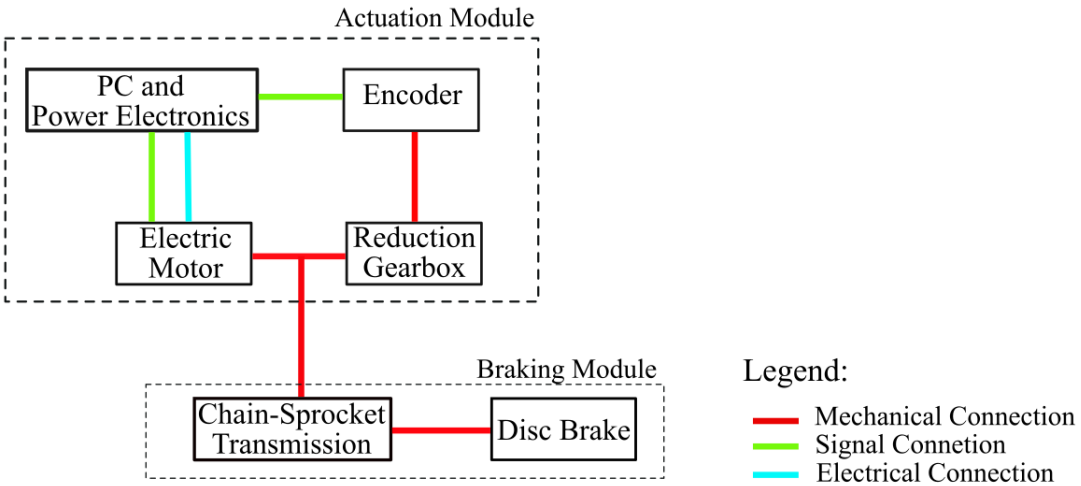

Figure 9: scheme of the test bench architecture

3.1 Actuation Module

The actuation module is composed by a mechanical reduction system connected to the Sinamic S120 AC/AC Trainer Package, a modular system able to perform high performance drive tasks. In the following chapters all the hardware components needed to design and develop the architecture of the actuation module, are going to be analysed by describing their characteristics and roles in the modular system. Part of the actuation module is highlighted in the sketch shown in *figure 10*.

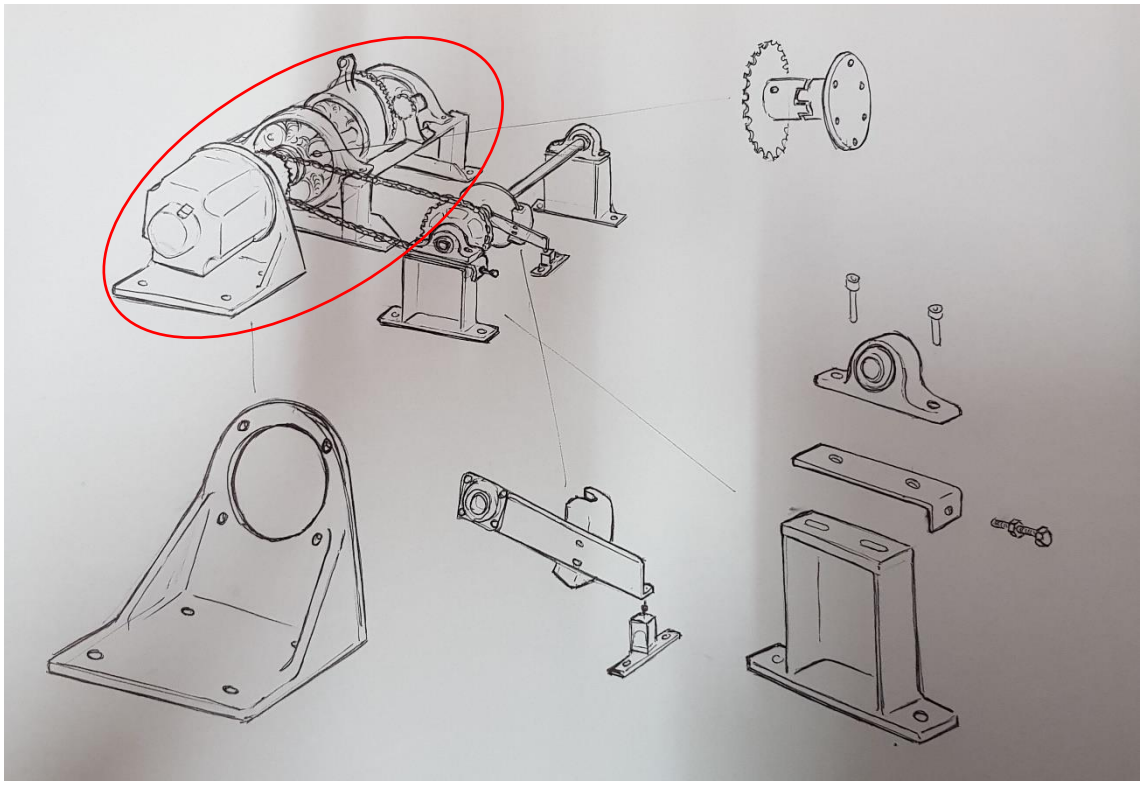

Figure 10: highlight of the actuation module in the first sketch

3.2 Hardware Components for the Actuation Module

3.2.1 Control Unit

The Control Unit CU310-2 PN made by Siemens is the “brain” on the system. It is a control module for single drives in which the open-loop and closed-loop control functions of the drive can be implemented. The Control Unit role is to give orders to the Power Module in the blocksize format to which is connected via the PM-IF interface located at the rear of the CU310-2 PN. The Control Unit is going to be mounted directly on the Power Module described in the next chapter. The Power Module chassis can be controlled from the Control Unit via the Drive-CliQ interface mounted next to the power module in the control cabinet. The CU310-2 PN is hot-pluggable which means that it can be easily replaced and is directly plugged to rest of the system without the need of any cables.

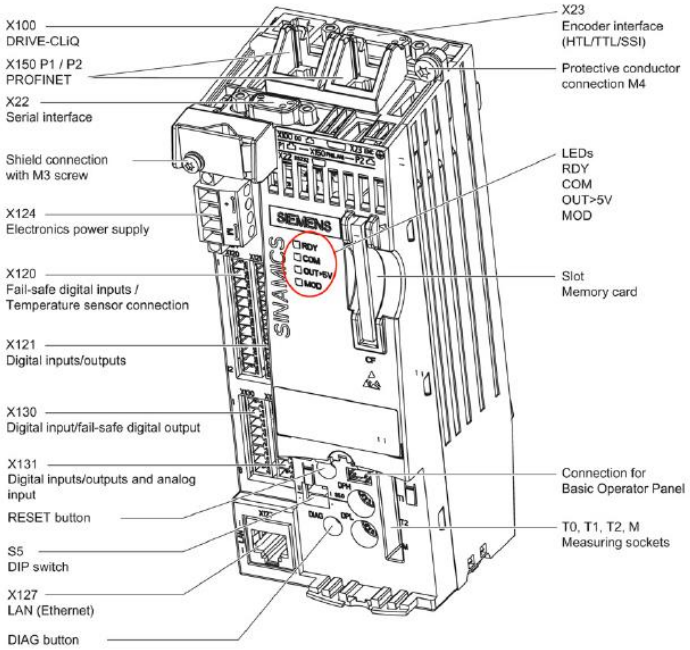

Figure 11: control unit overview of interfaces [2]

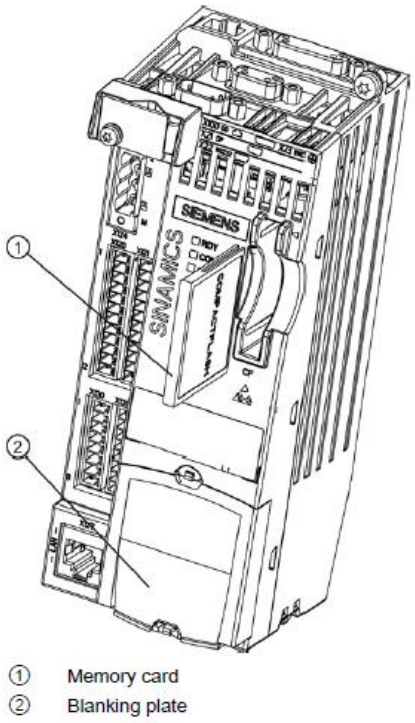

Figure 12: overview of the control unit compact flash card and its dedicated slot [2]

The control unit is also provided with a memory card slot able to host a CompactFlash Card with which the system is equipped.

3.2.2 Power Module

The Blocksize PM240-2 produced by Siemens is the Power Module,this components functions as an inverter and thereefore its core function is to power the motor's windings following the control laws given by the control unit. The main design features of this component are the following:

- Line-side diode rectifier
- DC-link electrolytic capacitors with pre-charging circuit
- Output inverter
- Braking chopper for (external) braking resistor
- 24 VDC / 1 A power supply
- Gating unit, actual value acquisition
- Fan to cool the power semiconductors

Figure 13: overview of the PM240-2 power module [2]

3.2.3 Basic Operator Panel

The system is provided with a BOP20 made by Siemens which is a basic operator panel with six keys a backlit display unit. This small panel can be plugged to the CU310-2 PN control unit to operate two main functions:

- Input of parameters and activation of functions
- Display of operating modes, parameters and faults

Figure 14: basic operator panel BOP20 [2]

3.2.4 Cables

There are two main cables utilized in the system:

- Power Cable: it transmits power to the motor and links the motor to the inverter
- Signal Cable: it transmits signals from the control unit to the motor so it can follow the actuation algorithm designed by the operator

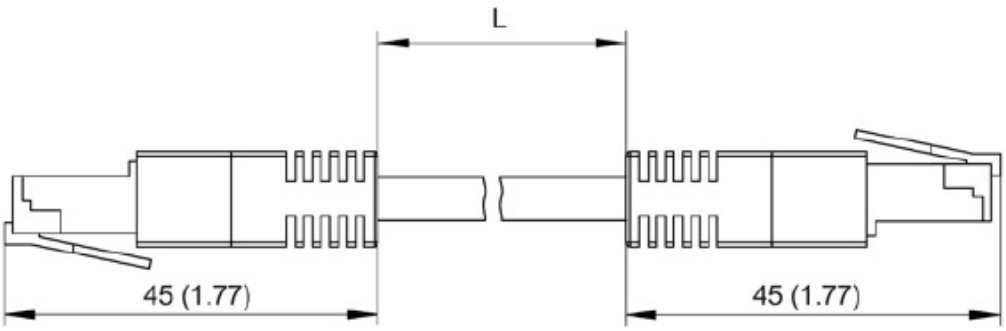

Figure 15:DRIVE-CLiQ signal cable [2]

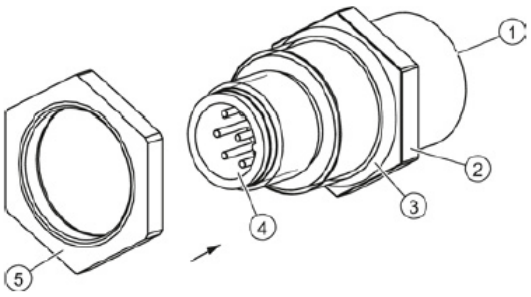

① DRIVE-CLiQ interface with M12 socket (8-pin)
② Flange, SW18
③ Seal
④ DRIVE-CLiQ interface with M12 plug (8-pin)
⑤ O ring, SW20, tightening torque: 3 to 4 Nm

Figure 16:overview of a DRIVE-CLiQ cabinet bushing M12[2]

3.2.5 Electric Motor

The electric motor has the role to drive the entire system during the simulation on the test bench. The motor, during the tests, is also going to be loaded by the braking module to simulate a resistant force on the actuator. During the tests the computer is going to keep track of motor behaviour to later develop closed loop control systems.

Figure 17: SIMOTICS synchronous motor 1FK7060-2AC71-1CG0[3]

The motor chosen to actuate the simulation is the SIMOTICS S Synchronous motor 1FK7060-2AC71-1CG0 (*figure 17*). This motor is built with the following features showed in the tables below:

Table 1: engineering data for the SIMOTICS S Synchronous electric motor[3]

Engineering Data	
Rated speed (100 K)	2000 rpm
Number of poles	8
Rated torque (100 K)	5.3 Nm
Rated current	3.0 A
Static torque (60 K)	5.00 Nm
Static torque (100 K)	6.0 Nm
Stall current (60 K)	2.55 A
Stall current (100 K)	3.15 A
Moment of inertia	7.700 $kgcm^2$
Efficiency	90.0%

Table 2: Physical constants for the SIMOTICS S Synchronous electric motor [3]

Physical constants	
Torque constant	1.1 Nm/A
Voltage constant at 20° C	121.0 V/1000*min^{-1}
Winding resistance at 20° C	2.75 Ω
Rotating field inductance	30.5 mH
Electrical time constant	11.10 ms
Mechanical time constant	1.75 ms
Thermal time constant	30 min
Shaft torsional stiffness	40500 Nm/rad
Net weight of the motor	7.1 kg

Table 3: Mechanical data for the SIMOTICS S synchronous electric motor [3]

Mechanical Data	
Motor type	Permanent-magnet synchronous motor
Shaft height	63
Cooling	Natural cooling
Radial runout tolerance	0.040 mm
Concentricity tolerance	0.10 mm
Axial runout tolerance	0.10 mm
Vibration severity grade	Grade A
Connector size	1
Degree of protection	IP64
Temperature monitoring	Pt1000 temperature sensor
Electrical connectors	Connectors for signals and power
Holding brake	without holding brake
Shaft extension	Plain shaft
Encoder system	Encoder AM24DQI: absolute encoder 24 bits (resolution 16777216, encoder-internal 2048 S/R) + 12 bits multi-turn (traversing range 4096 revolutions)

Table 4: Optimum operating points for the SIMOTICS S Synchronous electric motor [3]

Optimum Operating point	
Optimum Speed	2000 rpm
Optimum Power	1.1 kW

Table 5: Limit operating point for the SIMOTICS S synchronous electric motor [3]

Limiting Data	
Max permissible speed (mech.)	7200 rpm
Max permissible speed (inverter)	4750 rpm
Maximum torque	18.0 Nm
Maximum current	10.7 A

3.2.6 Motor support

A dedicated motor support was realized starting from the firs sketch of the system. The component was designed using Solidworks which helped to realize the 3D model of the motor support and its 2D drawing with all the measurements needed by the Ellena S.p.a factory to be crafted. The component was realized with a stell alloy.

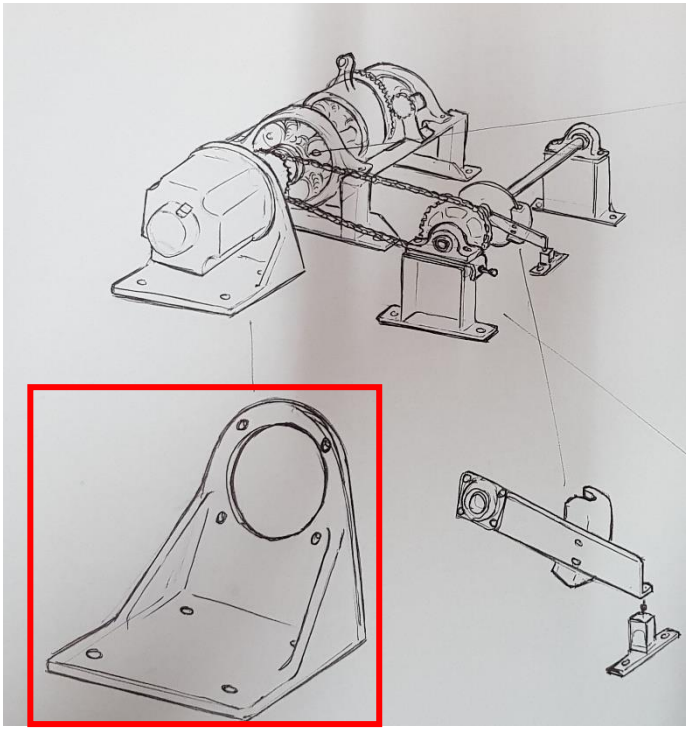

Figure 18: highlight of the first sketched motor support

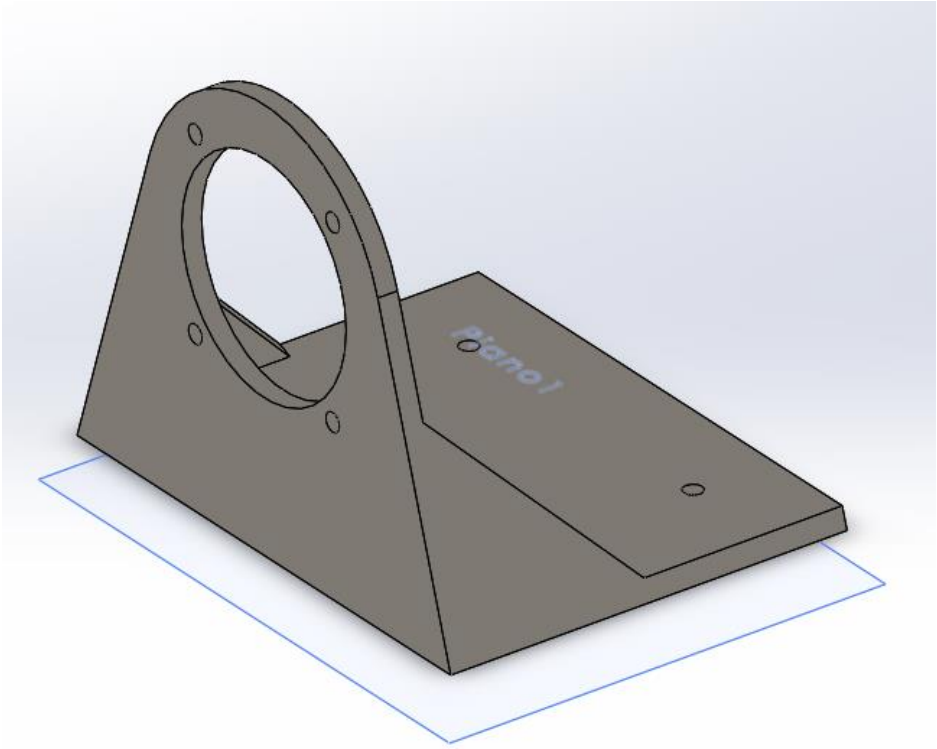

Figure 19: CAD model of the motor support

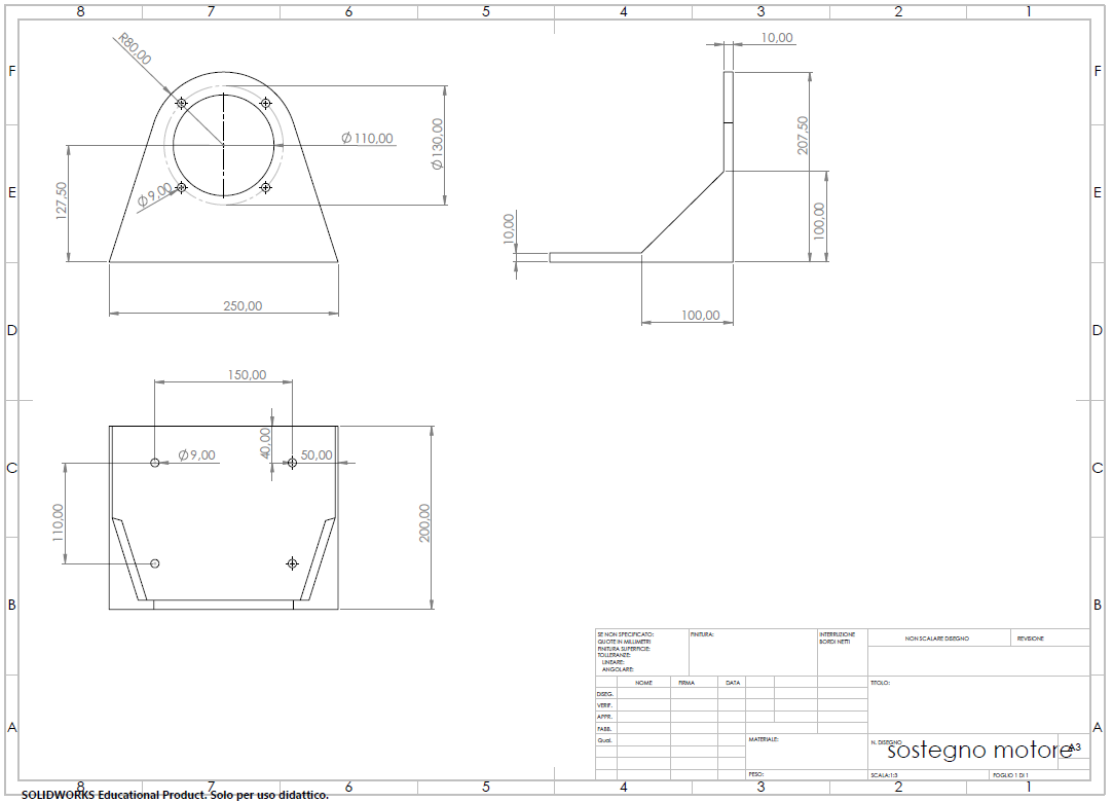

Figure 20: 2D drawing of the motor support

3.2.7 Reduction Stage

The reducer has the role of reducing the high-speed input coming from the electric motor shaft to a lower speed value.

The reducer employed in our test bench is a prototype realized by *Politecnico di Torino* with the use of Fused Deposition Modelling (FDM) additive manufacturing.

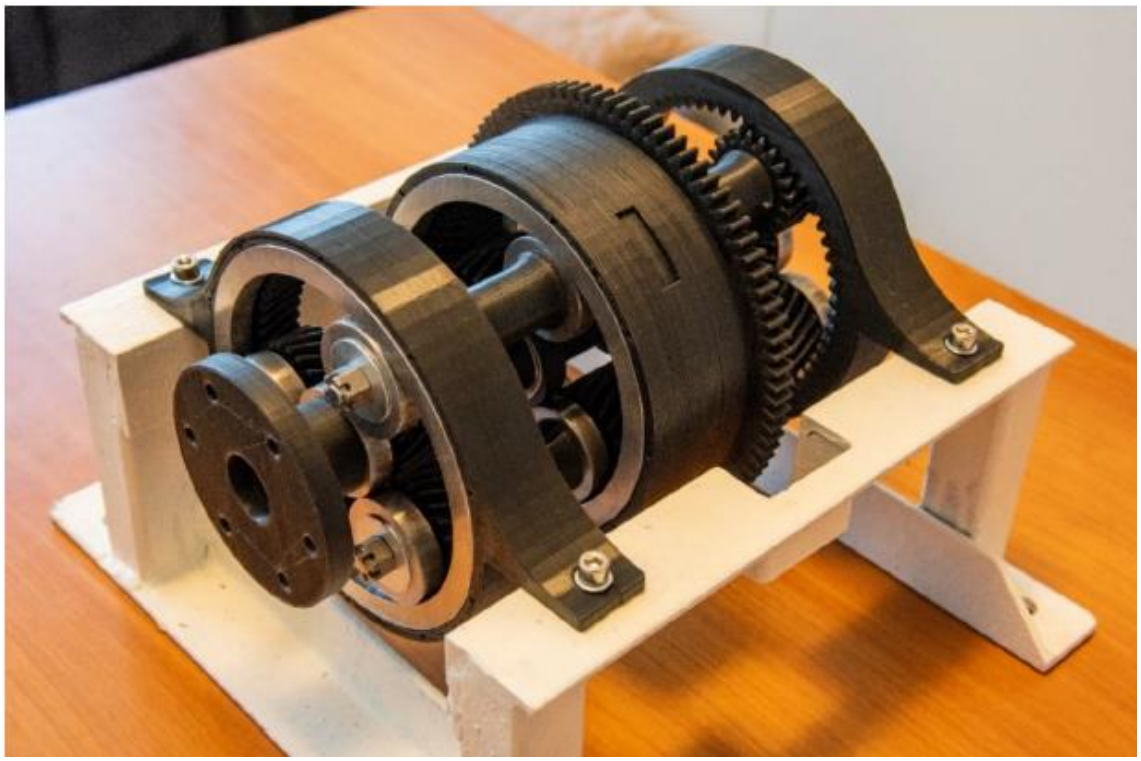

Figure 21: reduction gearbox utilized in the test bench [4]

The reduction gearbox is composed of four shaft three internal gears. The electric motor is going to be connected to an adapter placed at the end of the central shaft defined as "solar gear". The solar gear beside the adapter is composed of three spacers and two gear wheels with specular toothing angle and z_{S1} teeth each. The three external shafts are defined as "planetary gears" because of their motion around the central shaft and they dispose of z_{P1} teeth on the connection with the solar shaft and z_{P2} teeth for the gears connected with the output crown gear. Each one of the planetary gears is composed of two spacers and three gear wheels: the central wheel is designed with a double-helical toothing while the other two have a specular toothing angle. The entire assembly is held

by a steel alloy structure to which are fixed two stationary solars with internal gears and z_{S2} teeth.

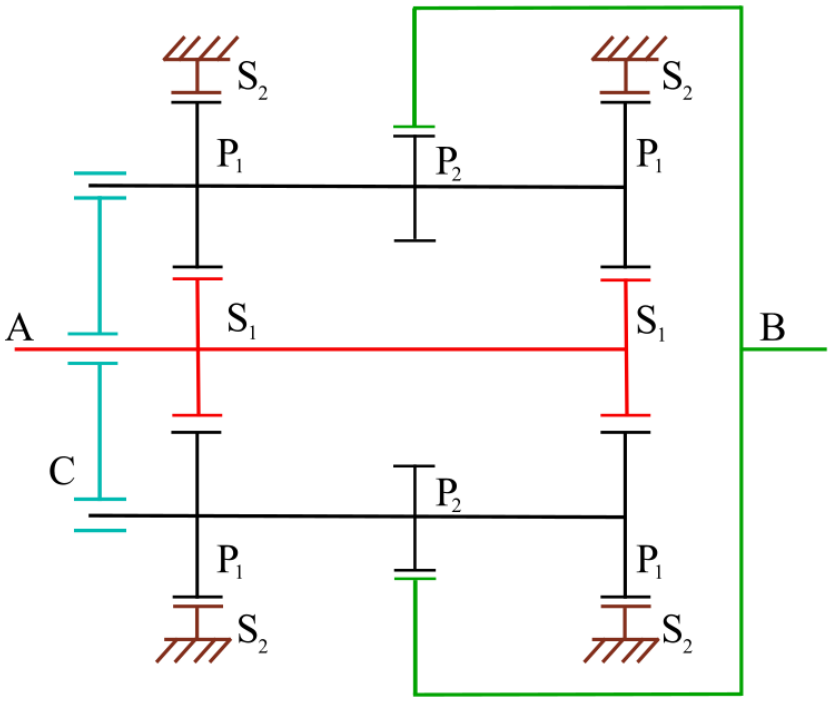

Figure 22: scheme of the reduction gearbox layout

In *figure 22* can be seen the global layout of the reducer and the connections between the different gears.

We can see that the central stage P_2 is engaging with the output crown gear B with z_B teeth. Since the number of teeth of stage P_1 is different from the number of teeth of stage P_2, the translation speed of the central planetary stage P_2 does not match its peripheral speed. In this way the reducer is going to transform an input speed V_A coming from the solar gear into an output speed:

$$V_B = \frac{V_A(R_{P1} - R_{P2})}{2 * R_{P1}}$$

Given the number of teeth for each gear, using the Willi's equation, the gear ratio of this transmission can be calculated. If the observer is set in reference system of the virtual planet carrier the transmission ratio from the input shaft A to the output crown B is:

$$\tau_1 = \frac{\omega_{S1} - \Omega}{\omega_B - \Omega} = -\frac{z_B z_{P1}}{z_{P2} z_{S1}}$$

Where Ω is the angular velocity of the planet carrier. Using the same method, also the transmission ratio τ_2 for the coupling of the input A and the stationary solar gears S_2 can be deducted, which is going to be:

$$\tau_2 = \frac{\omega_{S1} - \Omega}{\omega_{S2} - \Omega} = -\frac{z_{S2}}{z_{S1}}$$

Finally, if the stationary solar gears are imposed to be fixed, ω_{S2} is going to be null and the total gear ration in a fixed reference system is going to be:

$$\tau = \frac{\omega_{S1}}{\omega_{S2}} = \frac{1 + \frac{z_{S1}}{z_{S2}}}{\frac{z_{S1}}{z_{S2}} - \frac{z_{S1}}{Z_{P1}} \frac{z_{P2}}{z_B}}$$

3.2.8 Encoder

On the output crown gear of the reducer a high-resolution optical incremental encoder is placed so that it can measure the exact position of the output shaft and transmit the data to the computer to provide closed loop control. The position data can also be saved to be later analysed.

Figure 23: TSW581HS.M2.5000.5.V.K4.B127.PL10.PP2-5 optical incremental encoder [5]

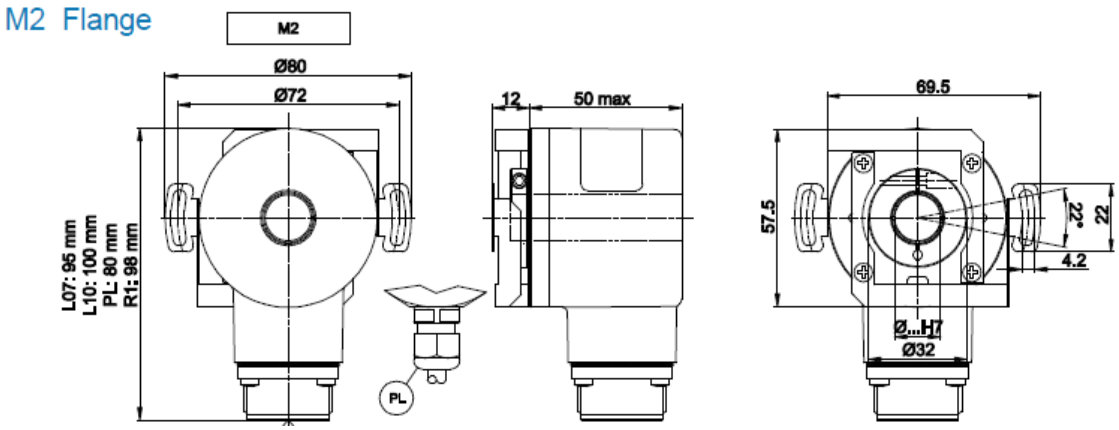

Figure 24: 2D drawing of the encoder [5]

The encoder used in this test bench is the TSW581HS.M2.5000.5.V.K4.B127.PL10.PP2-5 produced by Italsensors company. In *table 6*, shown below, can be seen the main features regarding the encoder with the explanation regarding its name mentioned before.

Table 6: main data about the optical encoder [5]

Model	TSW581HS	Bidirectional + index
Assembly	M2	M2 spring type
Pulse rate	5000	5000
Power Supply	5	5V ± 5%
Output frequency	V	From 0 a-up to 300 kHz
Protection Degree	K4	IP64 (EN60529)
Shaft	B127	12.7 mm of diameter
Electrical connection	PL10	Radial cable gland with cable 1m long
Output Circuits	PP2-5	Push-Pull 5V output only

Other features regarding the encoder used in the test bench are listed below in *tables 7, 8, 9 and 10.*

Table 7: materials regarding the main components of the optical encoder [5]

Materials	
Flange	Non corroding Aluminium
Housing	Polyamid 6 (PA6)
Shaft	Stainless steel

Table 8: Environmental specification regarding the optical encoder [5]

Environmental Specifications	
Operation temperature range	-10°C ÷ +70°C
Storage temperature range	-30°C ÷ +85°C
Relative humidity	98% RH without condensing
Vibrations	10 g (from 10 up to 2000 Hz)
Shock	20g (for 11 ms)

Table 9: Mechanical specifications regarding the optical encoder [5]

Mechanical specifications	
Shaft rotation Speed	6000 RPM continuous
Starting torque at 25°C	0.025 Nm
Bearings life	5 *10^9 revolutions (minimum)
Moment of inertia	40 g cm^2
Weight	~ 0.25 Kg

Table 10: electrical specificarions regarding the optical encoder [5]

Electrical Specifications	
Synchronous index output	Default on channel A;A+B optional
Supply Current without load	150 mA max
Protection	Short circuit protection (only output LD2 and PP2) against inversion of polarity(except 5V, 5/28 V)

3.2.9 Microbox PC

As an interface to control the SIMATIC system and visualize the operations through a dedicated software the Actuation module is provided with the SIMATIC IPC427E Microbox PC.

Figure 25: SIMATIC IPC427E Microbox PC [2]

This device is designed to provide industrial grade performances with a limited amount of space needed. Being specifically designed for engineering purposes this device is able to perform different kind of useful applications for the purposes of the test bench under design, like:

- Measuring and controlling all the processes and machine data
- Operating and visualizing different tasks
- Logging and processing data

In the following tables are shown the main features about the PC:

Table 11: basic data regarding the SIMOTIC microbox PC [2]

Basic Data	
Power supply	24 V DC (-20%/+20%) max. 4 A
Processor	Intel® Core™ i3-6102E Processor (3M Cache, 1.9 GHz)
Main Memory	16 GB DDR4-SDRAM SODIMM
Operative System	Windows Embedded Standard 7 SP1, 64 bit
SSD (Solid State Disk)	128 GB SATA
Graphic	HD graphic onboard
Installation	Installation on DIN rail, wall mounting or vertical mountig
Free slots for expansion cards	Up to 2 × PCIe cards

Table 12: ports provided on the SIMOTIC microbox PC [2]

Ports	
Serial	COM1 / COM2 (RS 232, RS 422, RS 485 configurable), optional
USB ports	4x USB V3.0 (high current)
Ethernet ports	3x Gbit Ethernet
Keyboard, mouse	Connected via external USB port
Graphics	2 x DisplayPort DPP (DVI via DP++ to DVI adapter possible)

3.3 Braking Module

3.4 First sketch

The braking module is the part of the system able to simulate and transmit a load force on the actuator. This module required a different design approach from the previous one since many components were not available on the market and had to be realized starting from sketches with the idea of adopting low cost materials.

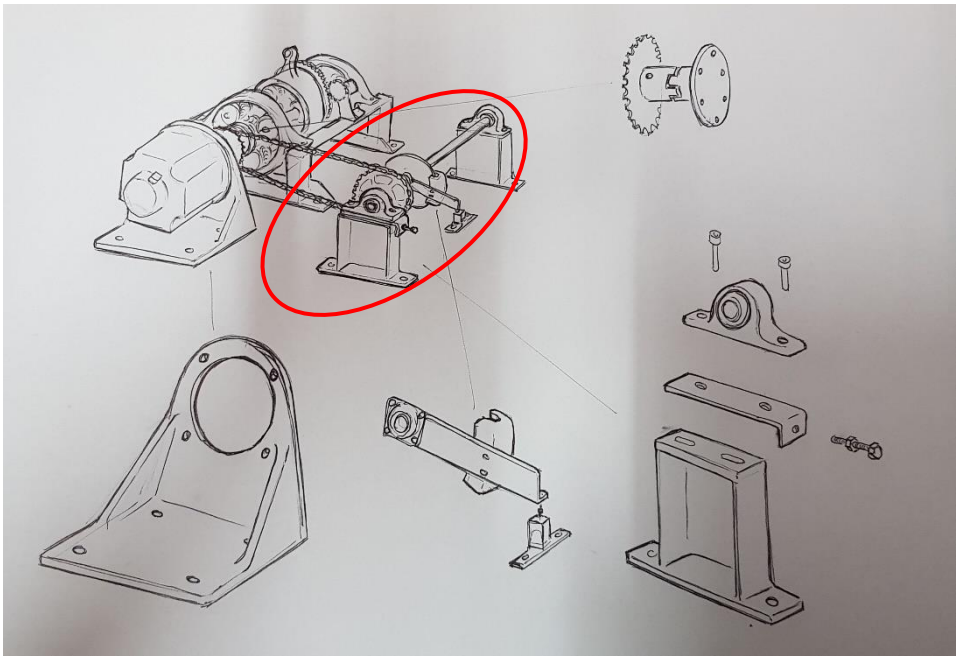

Figure 26: highlight of the braking module in the first sketch

As shown from *figure 26* above, to simulate the load on the motor, it was decided to have a shaft parallel the to the motor shaft. The shaft is placed on two iron supports and held by auto aligning bearings so it can rotate and allow a slight tolerance on the alignment of the supports. The shaft is designed with two different supports the first one is to host the sprocket for the chain transmission while the second one is designed to hold the brake disc. Next to the brake disk can be found an iron plate designed to support the brake and transmit the load force to a dedicated device able to measure the traction force and transmit it to a display to be visualized. The iron plate is connected to the shaft via two auto aligning bearings placed one on each side of the plate. The brake will be actuated

by a cheap modelling actuator via a steel cable that will permit to pull or release the brake lever.

3.5 CAD Model

The CAD model was realized starting from the sketch and its purpose was to design all the hardware that had to be crafted lately by the dedicated factory following the directions given by the 2D drawings. In *figure 27* is shown the final assembly obtained by matching all the different parts.

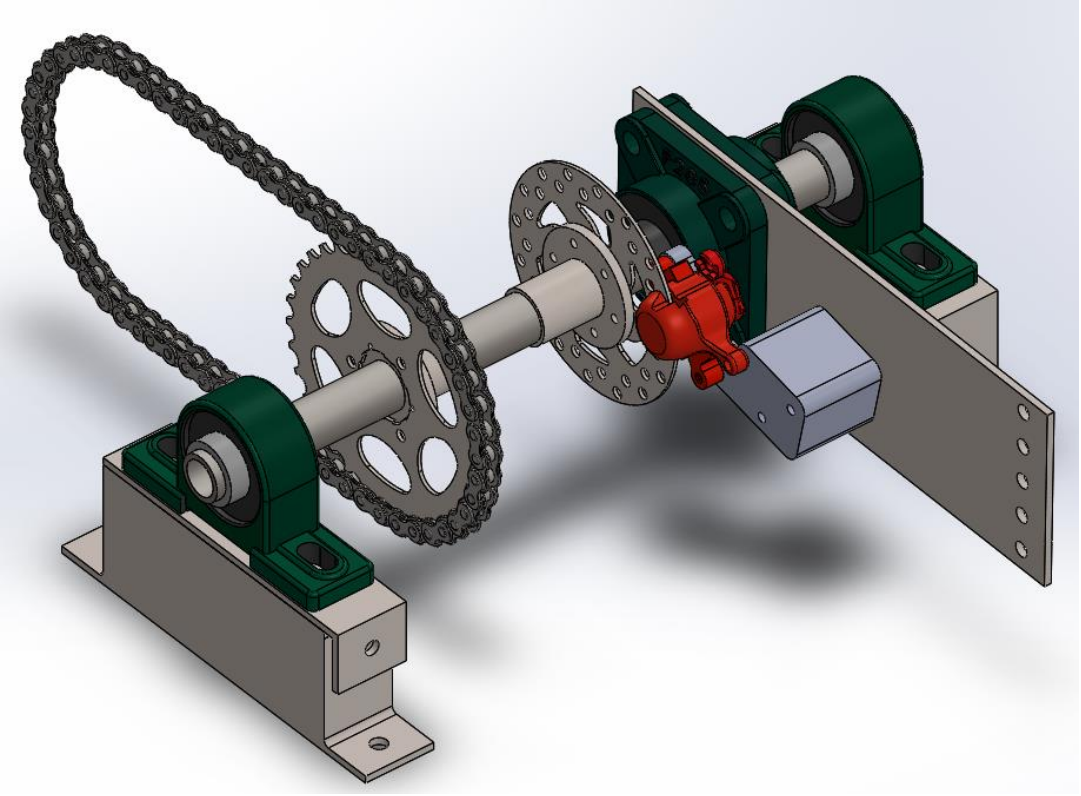

Figure 27: CAD assembly of the braking module

From *figure 27* it can be noticed that many components had to be modified or redesigned from the design shown in the sketch in *figure 26*. All the applied changes are going to be explained in following chapters which cover all the hardware that ad to be acquired or designed to assemble and define the architecture of the braking module.

3.6 Hardware Components for the Braking Module

3.6.1 The shaft' supports and the chain tensioner

The two supports, during the CAD modelling process, had to undergo some minor changes from the sketched design. With the help of the Solidworks software, the weight of the structure was estimated and some structural tests were done on the model to estimate the flexion of the vertical elements (*figure 28*) once they had to withstand the weight of the entire structure and the lateral tension of the chain once the motor will be running. After the tests it was decided to add a laminated vertical part to fill the hole at the centre of the support to make the whole structure more resistant and reduce its movement after the weight application (*figure 29*).

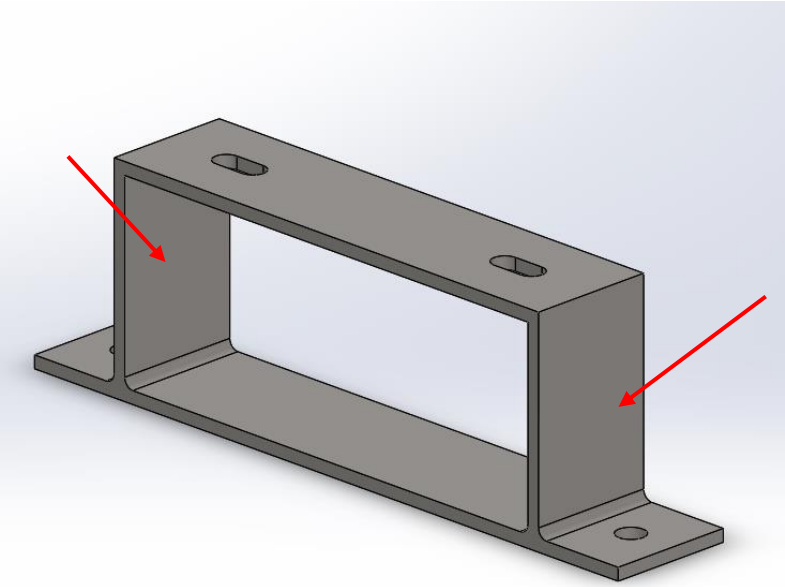

Figure 28: vertical parts of the support

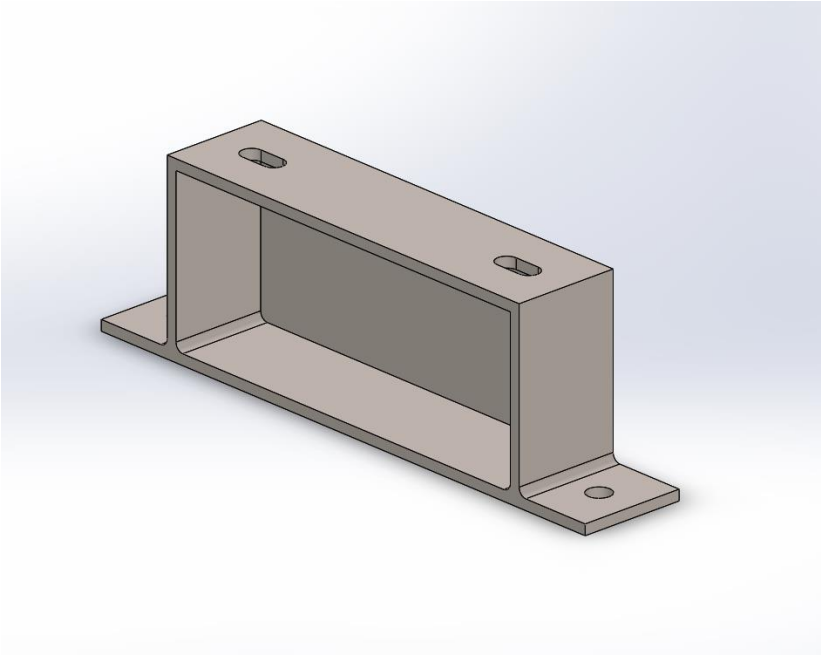

Figure 29: final CAD model of the support

The first displacement simulation was run estimating that each support will have to withstand half of the total structure weight. The software estimated the total weight of the structure at 5.395 kg but to be conservative the test were done with a total weight of 10 kg. During the simulation, a pressure of 8000 N/m^2 was applied on top of the support and the material was supposed to be a standard steel alloy. As it can be seen from *figure 30* and *figure 31*, which show the results obtained, it was possible to reduce both the overall displacement and the maximum displacement of the structure.

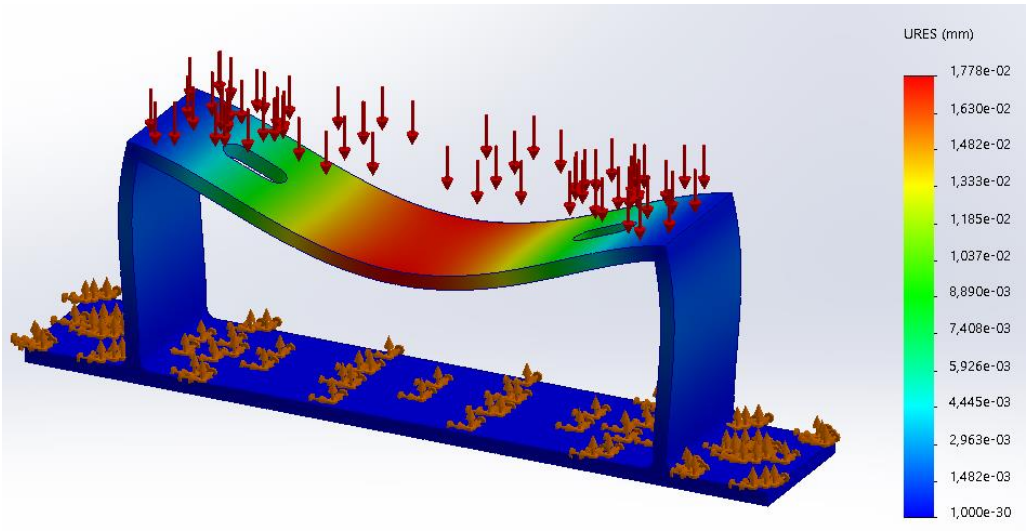

Figure 30: displacement results for the weight application on the support without central laminated part

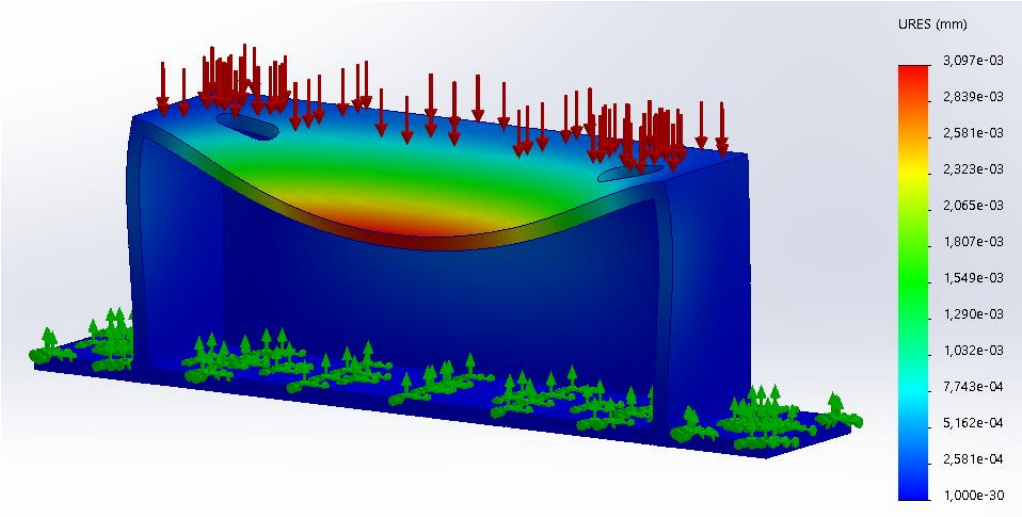

Figure 31: displacement results for the weight application on modified support

The second simulation was run adding to the pressure also a lateral force, which comes from the tension applied on the transmission chain, to also visualize the lateral displacement of the support. This force was estimated taking the maximum torque the electric motor on the bench could deliver (τ=*6 Nm*) and dividing it by the radius of the sprocket mounted on the motor shaft (*r=4.5 cm*).

$$T = \frac{\tau}{r} = 133.32N$$

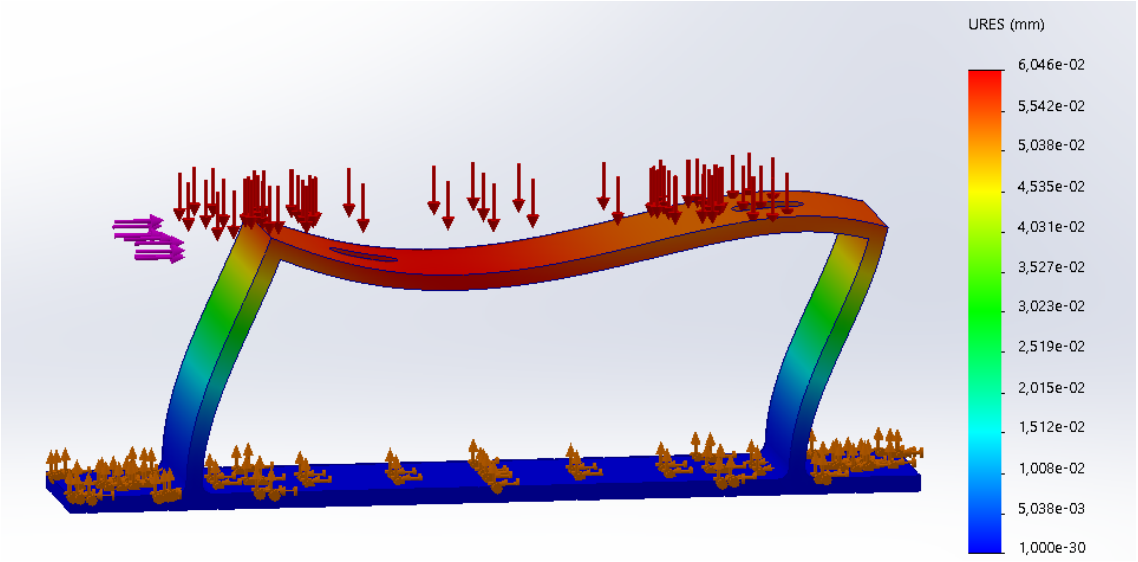

Figure 32: displacement results for the weight and tension application on the first version of the support

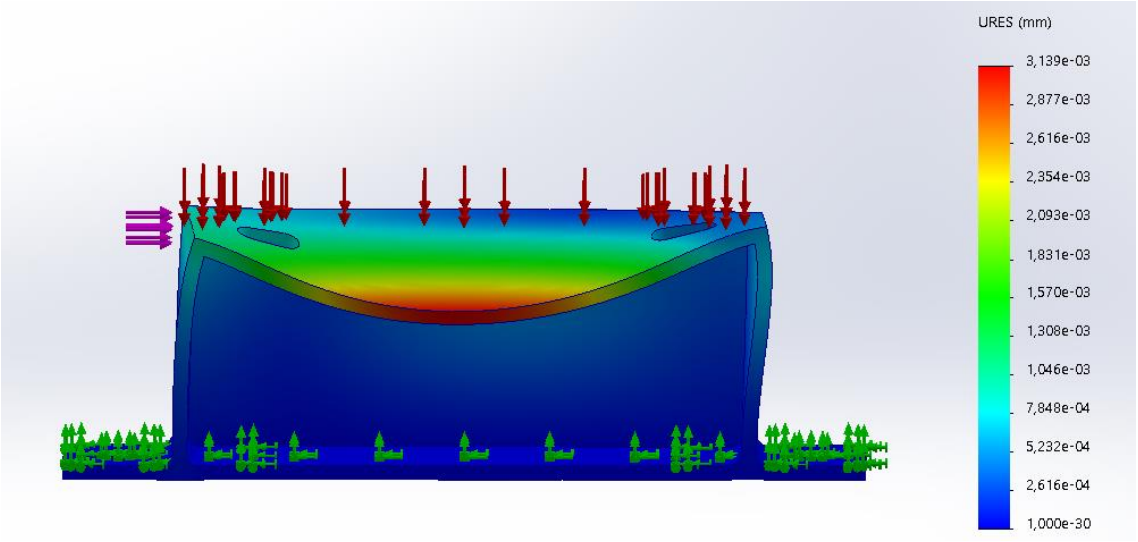

Figure 33: displacement results for the weight and tension application on the final version of the support

In *figure 32* and *figure 33* is shown the displacement obtained with the second structural simulation with both kind of supports. In the two figures mentioned above are also visible the advantages coming from the adjustments made on the supports: both the overall and maximum displacement of the structure were decreased giving to the entire system more stability and reliability.

Here in *figure 34* can be seen the 2D drawing, obtained from the 3D model, with all the data needed for the realization of this component:

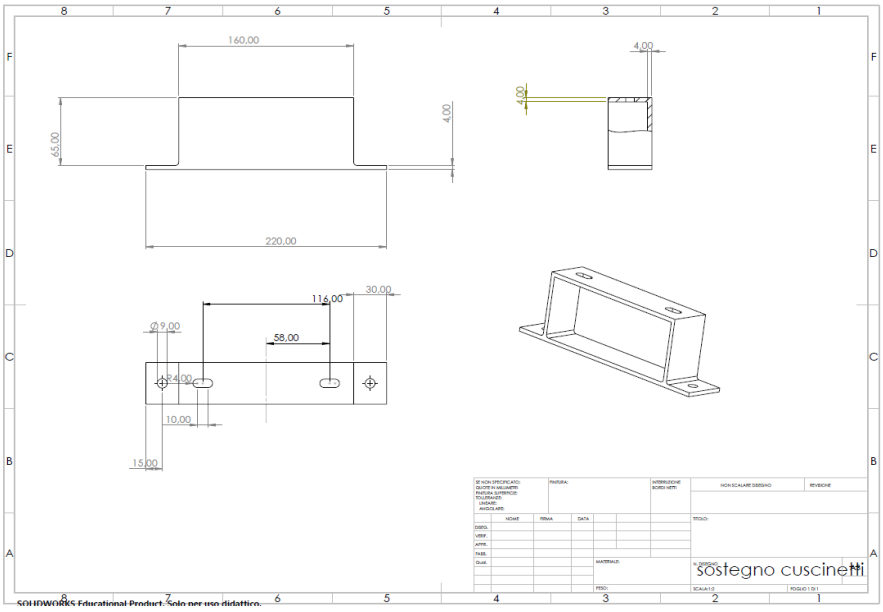

Figure 34: 2D drawing of the support

As shown in *figure 27*, on one of the supports, a steel device (*figure35*) can be seen placed under one of the bearings. That steel device was designed as a simple chain tensioner. The tensioner role is to shift the bearing by screwing a M8 screw, in this way a small force is going to be applied perpendicularly to the shaft axis which is going to create and maintain a certain desired tension on the trasmission chain. In this way the transmission chain be adjusted on the two sprockets to perfectly fit them and ensure a proper transmission.

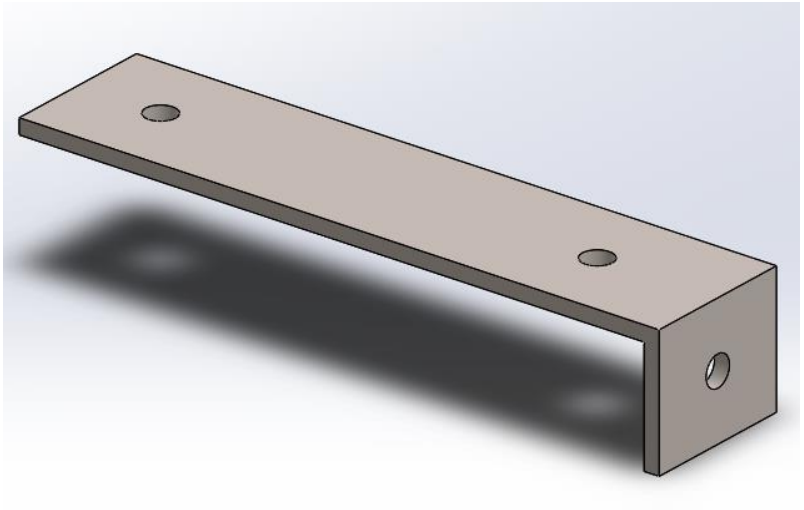

Figure 35: CAD model of the chain tensioner

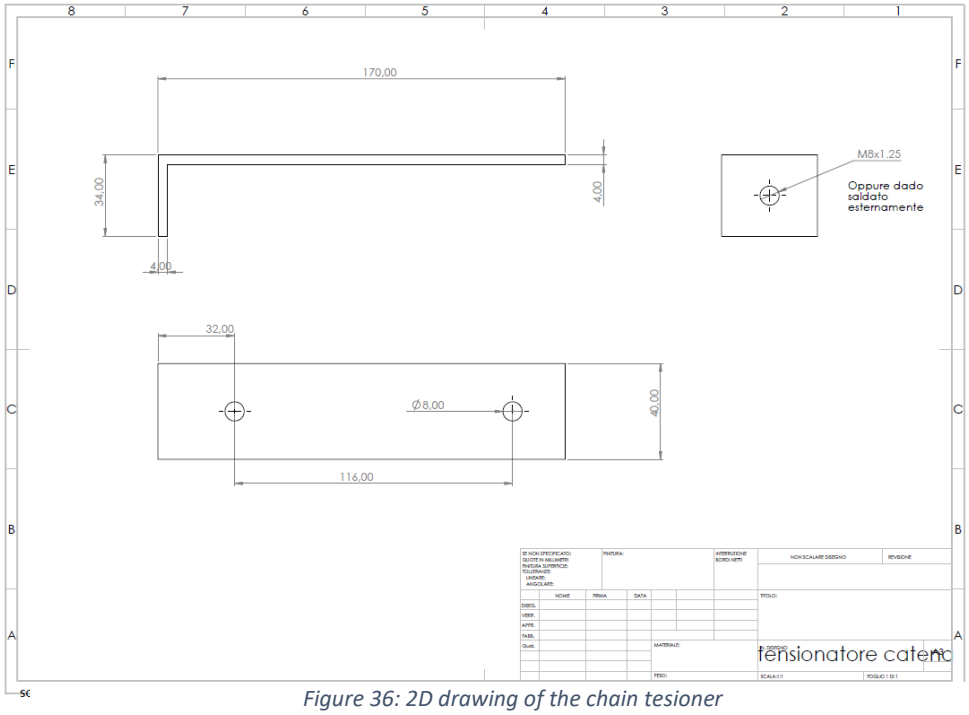

Figure 36: 2D drawing of the chain tesioner

3.6.2 The shaft

The shaft was designed with standard measures so it could fit the standard bearings available on the market. It's made of a steel alloy with 3 mm of thickness and 25 mm of diameter. As shownin *figure 38* two different supports directly welded on the shaft were designed so that the transmission sprocket and the braking disc could be firmly hosted.

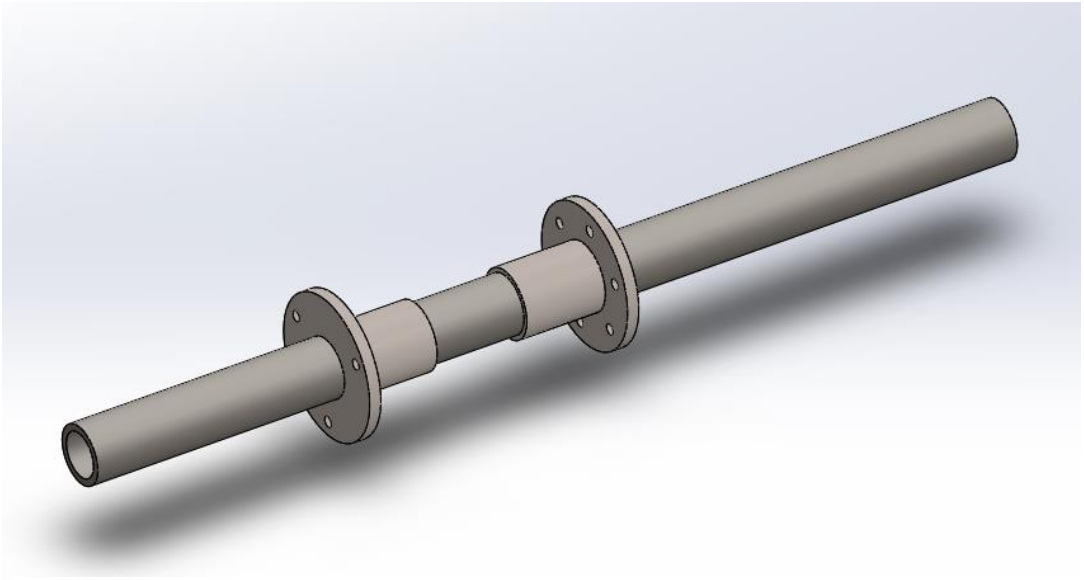

Figure 38: CAD model of the braking module shaft assembly

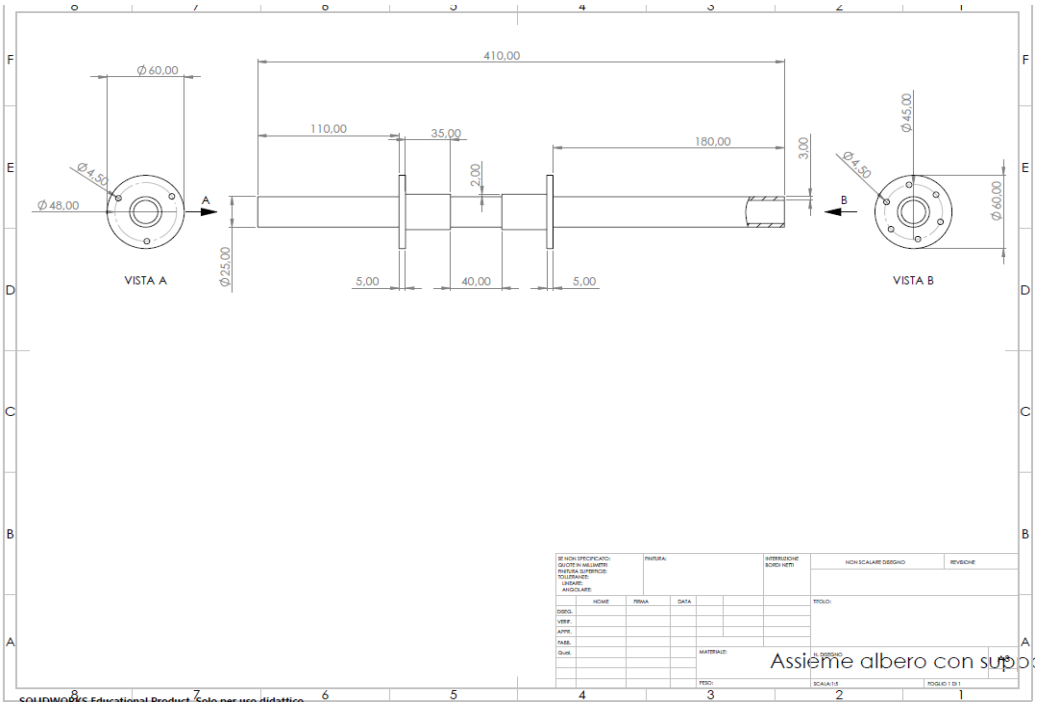

Figure 37: 2D drawing of the shaft

3.6.3 Bearings

The braking module required two couples of standard auto aligning 25 mm bearings. They were both acquired separately making sure they satisfied the requirements of reliability and low cost. As shown in *figure 27* the first couple of bearings (*figure 40*) is simply meant for sustaining the shaft and permit its rotation. The other couple of bearings (*figure 42*), close to the braking mechanism and attached to a rectangular steel plate, is meant to let the braking torque be transmitted to the load cell in order to be measured.

Both couples of bearings where transferred in the 3D model respecting all the relevant measurements made from the real component.

Figure 40: auto aligning bearing used on the test bench

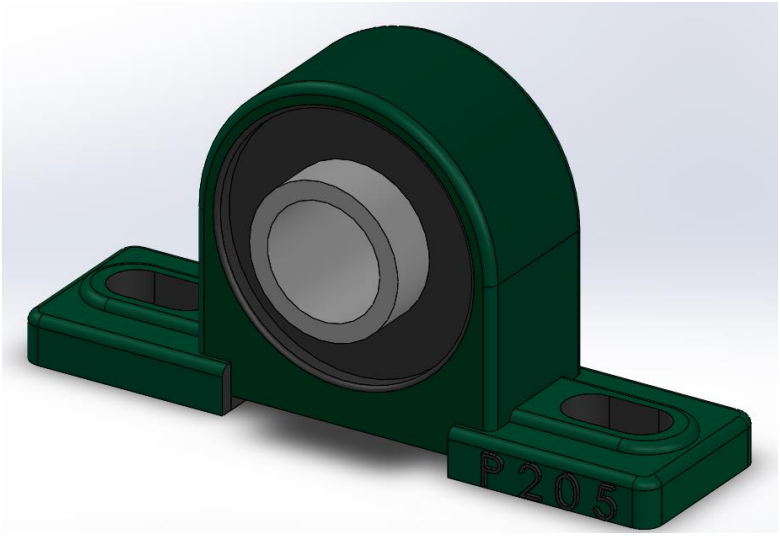

Figure 39: CAD model of the bearing

Figure 41: auto aligning bearing placed on the steel palate

Figure 42: CAD model of the bearing in figure 41

3.6.4 Braking Mechanism

With braking mechanism, is intended the specific system of elements involved in the application of the braking couple and the transmission of the charge to the load cell.

The brake is going to be actuated by the PDI-6221MG 20KG Large Torque Digital Standard Servo a small high torque standard servo actuator often used in the drone modelling sector (*figure 43*).

Figure 43: brake caliper actuator

This actuator can perform a 180° rotation applying a maximum stall torque of 20 Kg. In the *figure 44* and *table 13* are shown the main data and features of the utilized actuator:

Table 13: main data regarding the actuator

Description	
Brand	JX
Item name	PDI-6221MG 20KG Large Torque Digital Standard Servo
Degree	180°
Dead Band	2 µs

Working Frequence	500 µs/2500 Hz
Operating Speed (4.8V)	0.18 sec/85°
Operating Speed (6V)	0.16 sec/85°
Stall Torque (4.8V)	17.25 Kg*cm (239.55 oz/in)
Stall Torque (6V)	20.32 Kg*cm (281.89 oz/in)
Dimensions	40.5x20.2x38 mm
Weight	62 g
Connector Wire Lenght	265 mm
Bearing	2BB

Features:

- High performance digital standard servo
- High precision aluminium gears with hard anodizing
- CNC aluminium middle Shel
- Dual ball bearings

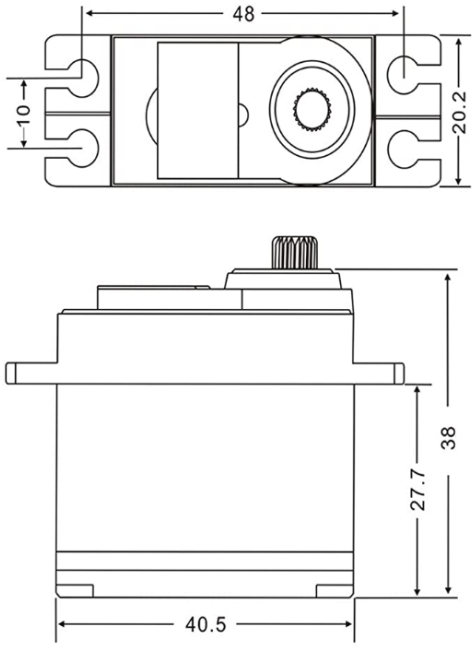

Figure 44: 2D drawing of the brake caliper actuator

The above actuator is going to pull a steel cable that is going to actuate the brake caliper assembly. In this way, by pulling the required lever, a piston is going to force the inner brake pads to squeeze to the disc brake surface creating friction and decelerating the shaft.

The brake it was decided to adopt for the purposes of the study (*figure 45*) is a standard disc brake often adopted in the cycling field. As shown in *figure 46* both the disc and the caliper were transferred in the CAD model respecting all the measurements relevant for the construction of the final assembly on the bench.

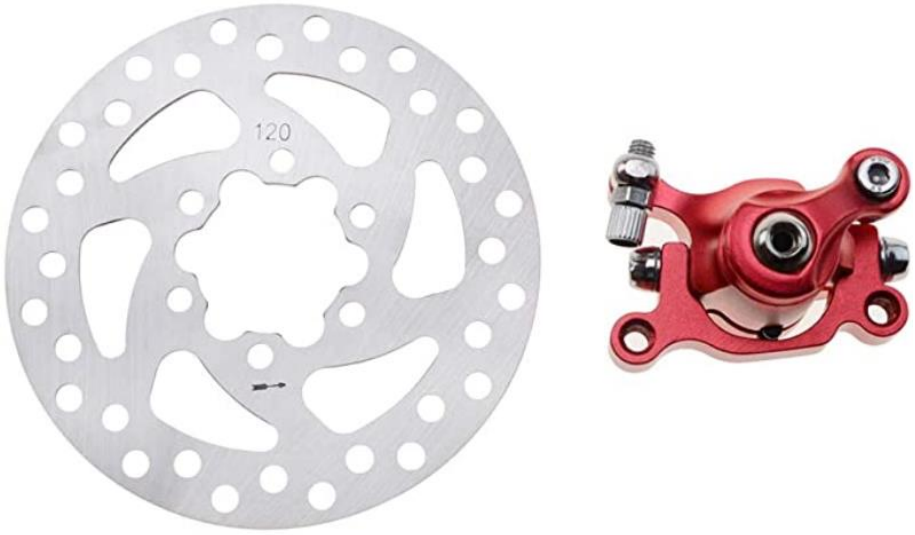

Figure 45: brake disc and caliper

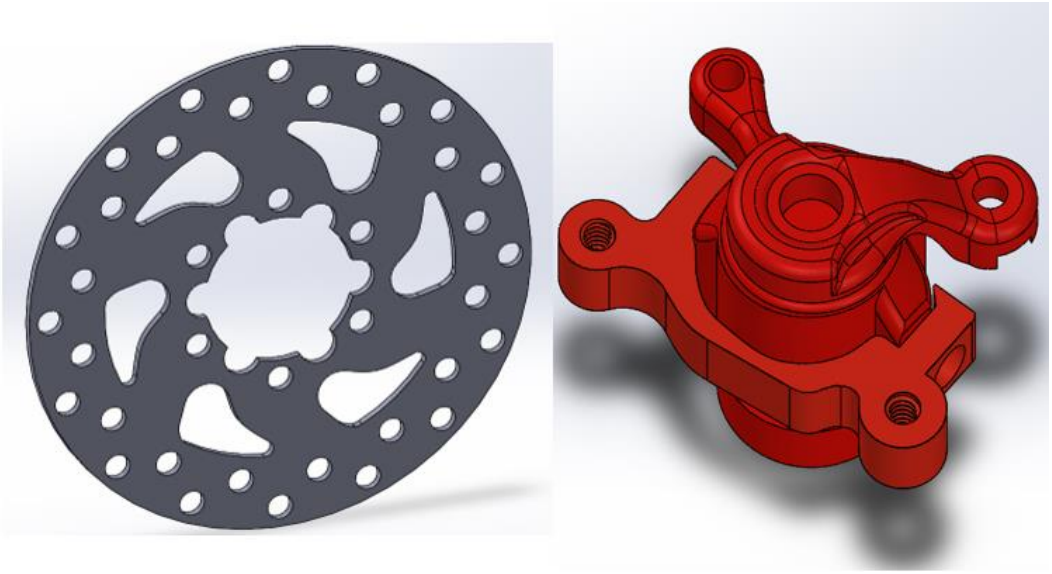

Figure 46: CAD model of brake disc and caliper

To proceed with the estimation of the braking momentum applied by the brake caliper it is better to introduce first the *Reye hypothesis* about the loss of material on the contact surfaces of two bodies in relative motion:

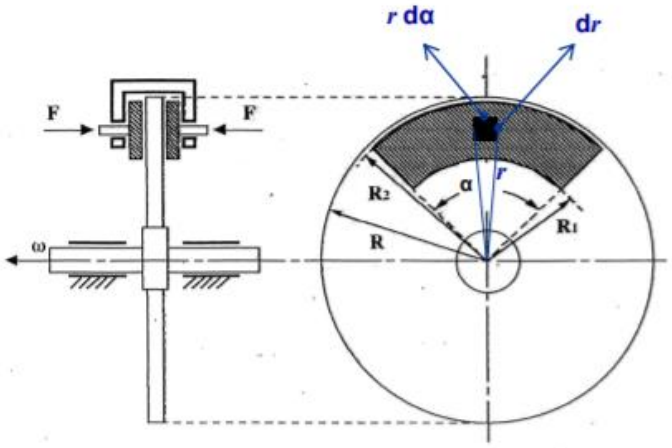

Figure 47: representation of a disc brake [6]

To measure the pressure distribution, it can be considered a rotating disc pushed to fixed disc. When the disc is new it is reasonable to assume that the pressure p would remain constant in all the contact points between the two elements. After a certain functioning time it can be noticed that the fixed disc made of dedicated friction material is going to show a thinner layer on the outer diameter. This phenomenon can be explained by a proportional hypothesis between the wear of the material and the work accomplished by the friction forces. The missing volume of material $d\mathcal{V}$ in a certain area dA that worn out in determined amount of time dt can be expressed by the following expression [6]:

$$d\mathcal{V} = d\delta * dA \tag{1}$$

Where $d\delta$ represents the thickness of the material that worn out over the dt time. The work done during the dt interval of time by the tangential contact due forces due to the friction is given by:

$$dL_f = f\ p\ dA\ V\ dt = f\ p\ \omega\ r\ dA\ dt \tag{2}$$

Where f represents the friction coefficient, p the pressure over an infinitesimal area dA of the contact zone and V the relative velocity between the two surfaces in considered area.

Making the hypothesis that dL_f is proportional to $d\mathcal{V}$:

$$dL_f = k\, d\mathcal{V} \tag{3}$$

Finally, it is obtained that:

$$\frac{d\delta}{dt} = \frac{f\omega r p}{k} \tag{4}$$

From the equation can be seen that since the friction constant f and the angular speed ω can both be considered constant quantities the material's wear out $\frac{d\delta}{dt}$ can be assumed proportional to the pressure p and to the distance from the axis of rotation r. If it is assumed being in the initial phases of the braking process, it can also be assumed the pressure to be constant over the surface and the unitary wear $\frac{d\delta}{dt}$ to vary only with the distance r. Over time the friction surface can be expected to wear out and the pressure is going to be greater toward the axis where the thickness of the pad is greater and lower toward the external diameter where the pad is going to be thinner.

If the motion of approach of the two surfaces is assumed to be a shift in the axial direction it can be supposed the wear out of the material to be uniform and therefore $\frac{d\delta}{dt}$ to be constant in all the contact points. Considering this last assumption about the overtime wear out process it can be stated that the pressure p is inversely proportional to the radius r:

$$p = \frac{k(\frac{d\delta}{dt})}{f\omega r} = \frac{k'}{r} \tag{5}$$

The hypothesis just used it's called Reye Hypothesis which states: "The volume V_{wear} of material lost for wear effects is proportional to the passive work L_p done by the friction forces producing that wear".

$$V_{wear} \propto L_p$$

The Reye hypothesis is not always valid in every circumstance, but it remains applicable and a really good mean of approximation in all the cases regarding dry friction between two surfaces that get in contact.

Now, if it is considered valid the Reye Hypothesis, also the intensity of the global normal force acting on the brake disc can be determined.

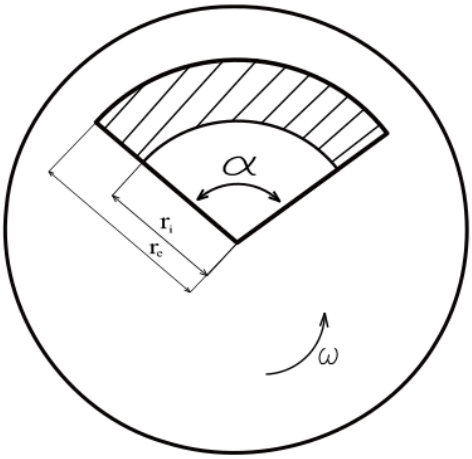

Figure 48: representation of brake disc with

If it is considered r_i and r_e as the internal and external radius of the contact surface, α the opening angle of this surface (*figure 48*) with r and θ the polar coordinates of the generic contact point the following expression for the global normal force can be obtained:

$$F_n = \int_{r_i}^{r_e} \int_{-\alpha/2}^{+\alpha/2} p\, r\, dr\, d\theta = k\, \alpha\, (r_e - r_i)$$

The sum of all the tangential force actin in every point of the raking pad will also generate a global braking momentum that can expressed with the following equation:

$$M_f = \int_{r_i}^{r_e} \int_{-\alpha/2}^{+\alpha/2} f\ p\ r^2\ dr\ \ d\theta = f\ k \frac{\alpha}{2} (r_e^2 - r_i^2)$$

If it is taken the expression of *k* from *equation 5* the final relation about the global friction momentum will be obtained:

$$M_f = f\ F_n\ \frac{r_e + r_i}{2}$$

The maximum value of pressure in the contact zone is going to be:

$$p_{max} = \frac{k}{r_i} = \frac{F_n}{\alpha\ r_i (r_e - r_i)}$$

In our specific case the brake pad is circular, and the brake disc has holes distributed on its surface to help the cooling and avoid the overheating of the disc. Since the brake disc is rotating while the system is operating, to ease the estimation of the braking force and momentum, the assumption of having a disc without holes was made and therefore the contact area is going to be the whole area of the circular pad.

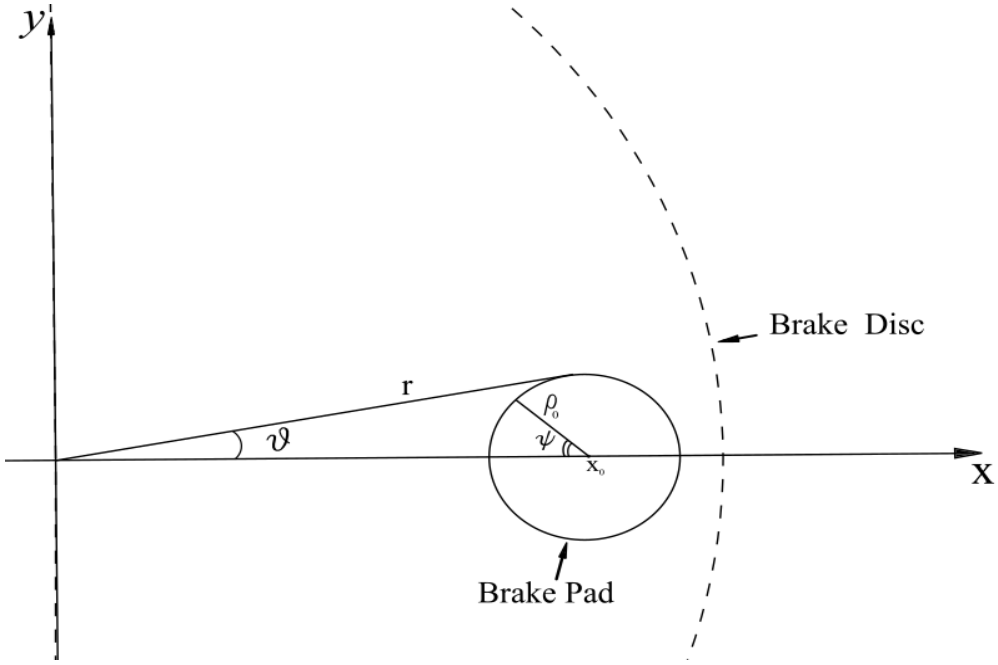

Figure 49: representation of a brake disc and brake pad on a Cartesian plane

To estimate the global normal force and braking momentum with a circular area it had to be introduced a different set of constant values and variables to estimate the area with respect to the distance from the centre of the brake disc (*figure 49*):

- ρ_0: the radius of the circular pad
- x_0: the x coordinate of the centre of the braking pad circumference also indicating the distance between the braking pad and the brake disc centers
- ψ: the angle between the radius of the pad and the x axis
- the x coordinate of the circumference points

$$x = x_0 + \rho_0 \cos(\pi - \psi)$$

- the y coordinate of the circumference points

$$y = \rho_0 \sin(\pi - \psi)$$

- the r variable indicating the distance of each contact point from the centre of the braking disc

$$r = \sqrt{x_0^2 + \rho_0^2 cos^2(\pi - \psi) + 2x_0\rho_0 \cos(\pi - \psi) + \rho_0^2 sin^2(\pi - \psi)}$$

- the angle θ between *r* and the x axis

$$\theta = \text{atan}\left(\frac{\rho_0 sin(\pi - \psi)}{x_0 + \rho_0 \cos(\pi - \psi)}\right)$$

The integral equation of the global normal braking force is going to be:

$$F_n = 2\int_{x_0-\rho_0}^{x_0+\rho_0}\int_0^{\theta_{max}(r)} p\, r\, dr\, d\,\theta =$$

Since the relation $p = {}^{k}/_{r}$ was already determined

$$F_n = 2k\int_{x_0-\rho_0}^{x_0+\rho_0}\int_0^{\theta_{max}(r)} dr\, d\theta =$$

$$= 2k\int_{x_0-\rho_0}^{x_0+\rho_0} \theta_{max}(r) dr =$$

By operating a change of variables

$$F_n = 2k \int_0^{\pi} \theta_{max}(\psi)\, dr(\psi) =$$

$$= 2k \int_0^{\pi} \operatorname{atan}\left(\frac{\rho_0 \sin(\pi - \psi)}{x_0 + \rho_0 \cos(\pi - \psi)}\right) * \frac{\sin(\psi)[(x_0 - \rho_0)(x_0 + \rho_0)\cos(\psi) + \rho_0 x_0]}{\sqrt{x_0^2 sin^2(\psi) + [x_0 - \rho_0 \cos(\psi)]^2}} * d\psi$$

The integral equation to find the global braking momentum with a circular pad is going to be:

$$M_n = 2 \int_{x_0 - \rho_0}^{x_0 + \rho_0} \int_0^{\theta_{max}(r)} fpr^2 dr d\theta$$

By operating the previously seen substitution of *p* and the change of variable form *r* to ψ, the integral equation is going to be:

$$M_n = 2fk \int_0^{\pi} r(\psi)\, \theta_{max}(\psi)\, dr(\psi) =$$

$$= 2fk \int_0^{\pi} \frac{\sqrt{x_0^2 + \rho_0^2 cos^2(\pi - \psi) + 2x_0\rho_0 \cos(\pi - \psi) + \rho_0^2 sin^2(\pi - \psi)}}{\sqrt{x_0^2 sin^2(\psi) + [x_0 - \rho_0 \cos(\psi)]^2}}$$

$$* \operatorname{atan}\left(\frac{\rho_0 \sin(\pi - \psi)}{x_0 + \rho_0 \cos(\pi - \psi)}\right) *$$

$$* \sin(\psi)\, [(x_0 - \rho_0)(x_0 + \rho_0)\cos(\psi) + \rho_0 x_0]\, d\psi$$

To evaluate the numerical value of both the braking force and braking momentum the Matlab script shown in *figure 50* has been developed. Once all constant values and variables were determined the function *trapz* was used to determine the numerical value of the integral equation by the trapezoidal numerical integration method.

```
clear all
close all
clc

rho_0=8.5e-3;
x_0=51.5e-3;
k=1;
f=0.6;
psi=linspace(0,pi,1000);
x=x_0+rho_0*cos(pi-psi);
y=rho_0*sin(pi-psi);
r=sqrt(x.^2+y.^2);
theta=atan(y./x);
figure
plot(x,y)
figure
polarplot(theta,r)
FN=2*k*trapz(r,theta)
MN=2*k*f*trapz(r,r.*theta)
```

```
FN =

    0.0044

MN =

   1.3619e-04
```

Figure 50: Matlab script to find global brake force and momentum

As shown in *figure 50* the results obtained were found with a unitary value of the constant *k* and a friction coefficient of 0.6. The script can be easily adjusted for any different set up situation which involves a circular braking pad.

When a braking force is applied thanks to the bearings and the plate to which the brake caliper is connected the braking force will be transmitted to a charge cell.

The body of the cell is functioning just like a spring, attached to the body can be found a dedicated extensometer sensor that can detect the mechanical deformation of the body once the body is undergoing a tension force. This electric extensometer is essentially an electric resistance attached to the to body' surface, when the body is deformed the wire will follow this deformation and change its length and therefore its resistance value. This change in resistance will be detected by a circuit to which the cell is connected. Knowing the mechanical physical characteristics of the material this signal can finally give us the force pulling the charge cell.

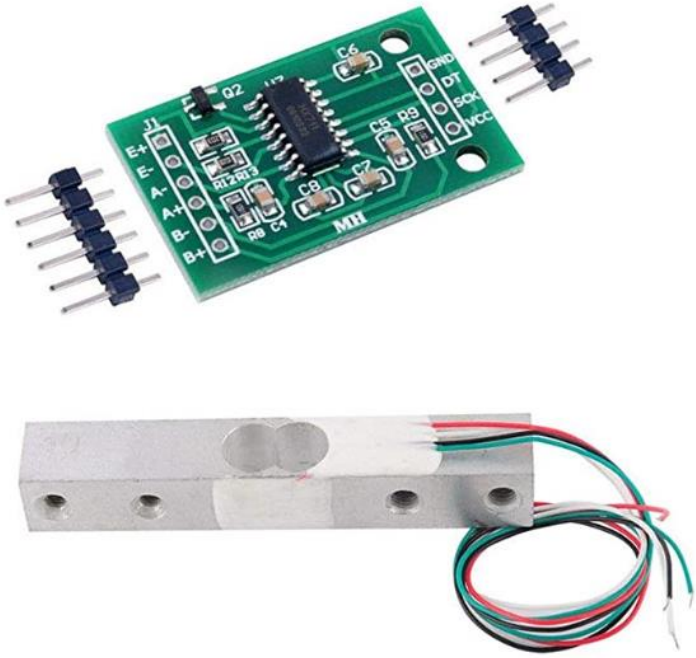

Figure 51: charge cell components

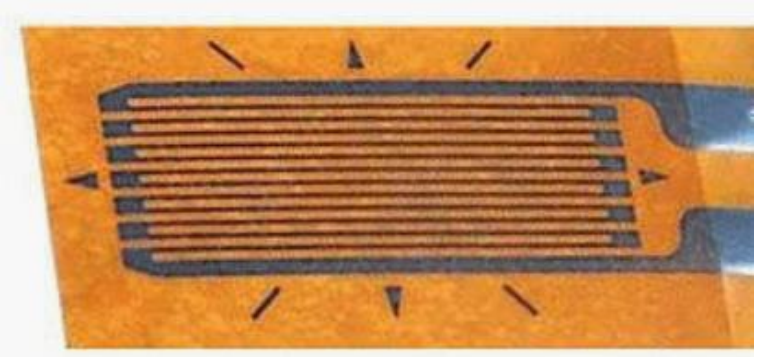

Figure 52: standard electric extensometer

Once known the value of the force registered by the charge cell, the force con be multiplied by the distance between the point of application of this force and the rotation axis of the shaft. This product will give the exact value of the braking torque applied on the shaft. As shown in *figure 53* the distance between the point of application and the rotation axis is 223 mm.

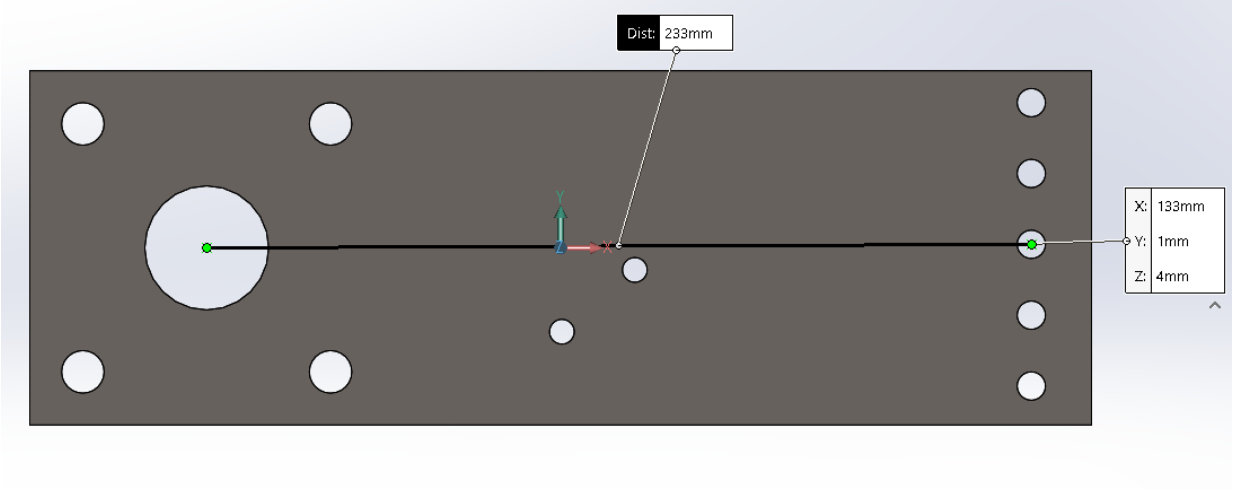

Figure 53: CAD model of the steel plate

3.6.5 3D Printed plastic junction

As shown in *figure 54* a plastic junction had to be designed so that the braking momentum could be transmitted from the brake caliper to the steel plate.

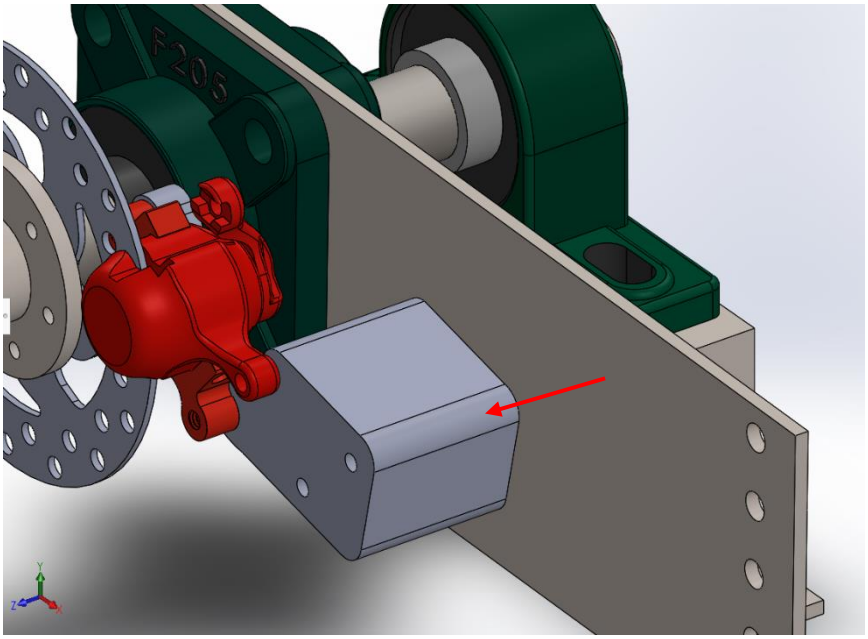

Figure 54: overview of the brake module assembly with highlight on the 3D printed plastic junction

The unusual shape of the junction, shown in *figure 55* was achieved to follow at its best the outer shape of the brake caliper and fill the gap between the caliper and the plate avoiding the contact between the caliper and the bearing.

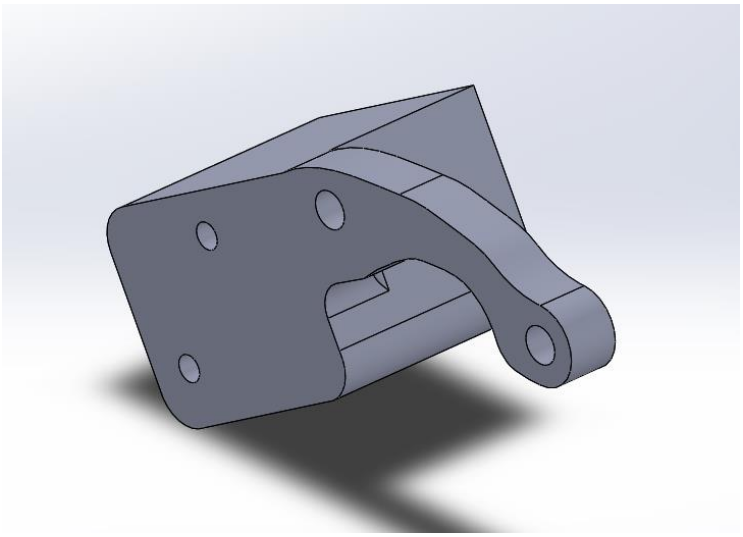

Figure 55: CAD model of the junction

3.7 Torque Transmission

The actuation module and the braking module are connected via a chain sprocket transmission, in this way power is transferred through a drive train from one sprocket to another through the tension created on a chain wrapped around the two sprockets. Therefore, the transmission chain allows torque to be transmitted in both ways. The electric motor torque can be transmitted to the braking module shaft which can freely rotate around its axis thanks to the bearing supports, and vice versa, through the same transmission chain, a braking torque can be transmitted to the motor when the braking system is actuated.

The chain used for the transmission is a simple roller chain, the same kind of chain that can be found on bicycle, motorcycle, and various kind of machine tools. In *figure 56* can be seen a portion of a standard roller chain with pin links.

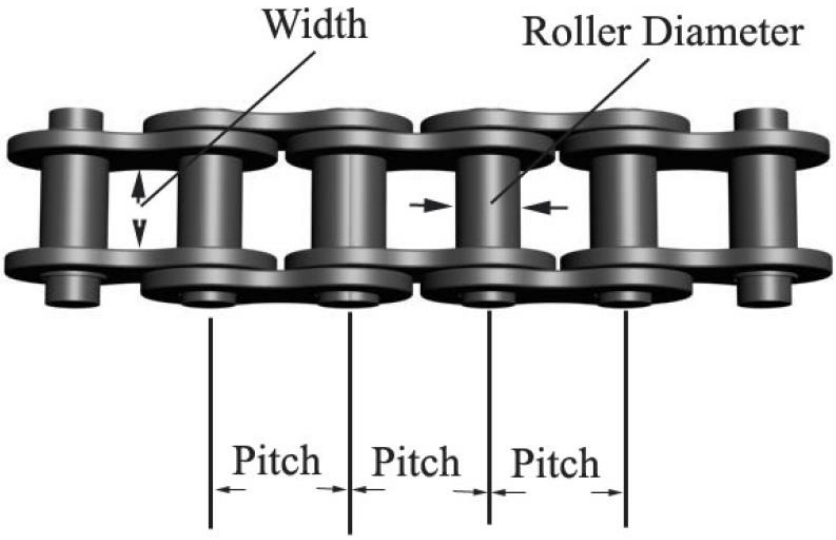

Figure 56: section overview of a transmission chain with its components [7]

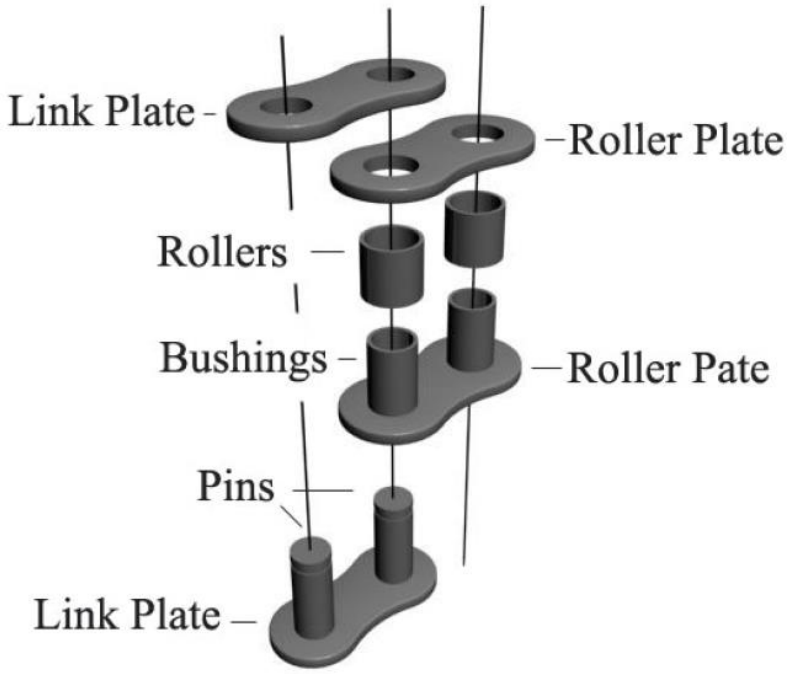

Figure 57: exploded view of a roller link [7]

As shown in *figure 57* in a roller link, two rollers can be found. The roollers can roll on two bushings. The two bushings are press fitted into two link plates. The complete pin link is composed by two pins fitted into two link plates.

To let the chain smoothly work during the transmission process an accurate lubrification is going to be essential. An accurate lubrification of the chain can also reduce the noise and enable a longer operational life of the chain.

The two sprockets utilized for the chain drive transmission can be seen in *figure 58* and *figure 59*.

Figure 58: driving sprocket

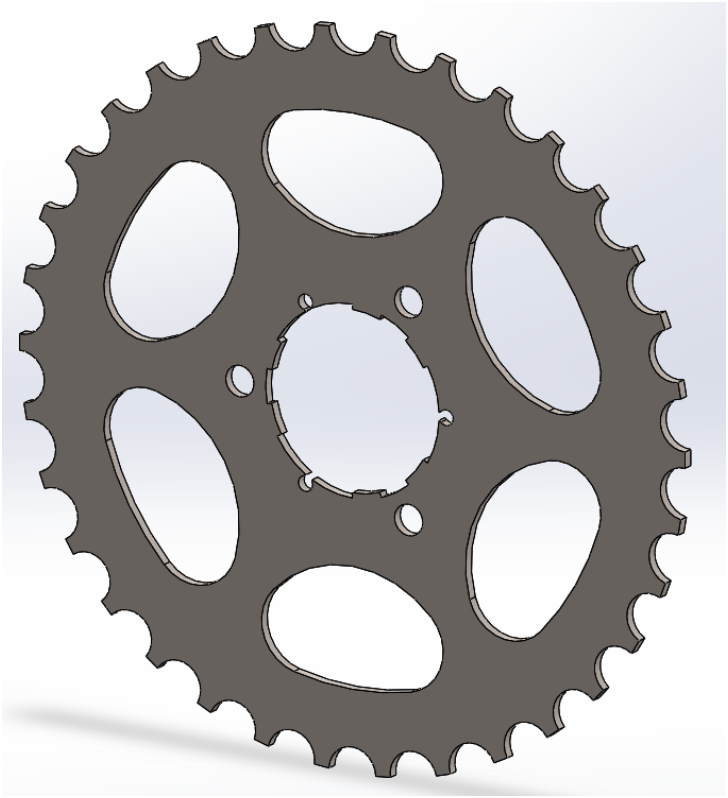

Figure 59: CAD model of the driven sprocket

The driving sprocket, in *figure 58*, has a diameter of 9 cm and it features 23 teeth, while the driven sprocket in *figure 59* has a diameter of 14.2 cm and is provided with 34 teeth. The sprocket ratio is 1.48, this means the drive sprocket must turn 1.48 revolutions before the driven sprocket turns 1 this way, the velocity can be reduced, and the torque increased on the driven sprocket. The drive ratio is the relationship between the number of teeth of the driven sprocket and drive sprocket and is equal to the relationship between the velocities (RPM) of the two involved shafts.

$$Drive\ Ratio = \frac{driven\ sprocket\ teeth}{drive\ sprocke\ tteeth} = \frac{\omega_{drive}}{\omega_{driven}} = \frac{34}{23} = 1.48$$

But the main reason for introducing a drive ratio instead of using two identical sprockets was to make the braking test more repeatable. The brake caliper and disc at disposal are both designed for small scooters and bicycles and this means that the braking torque the brake is able to apply is going to be around 20÷30 *Nm* while our electric motor stall torque is *6 Nm*. This means that to not reach the stall torque the brake would have to work way under its working range. For this kind of mechanical instrument having to work under its range of capabilities means also being more liable to a wide range possible random errors, from the mechanical ones to environmental errors. Having a drive ratio of 1.48 will allow the electric motor to feel a lower braking torque than the one actually applied by the brake. Therefore, the brake is going to be able to work more in the middle of its working range granting a better repeatability of the experiments.

The choice of simulating a load on the motor through a chain transmission instead of having the brake mounted on the motor' shaft, beside introducing a drive ratio with the previously said deriving advantages, was also adopted to introduce a certain amount of play between the two sprockets. By simply acting on the chain tensioner the chain can be loosened and introduce a delay in the motor response to the load. The primary function of this delay is to better simulate the real response of an onboard electromechanical actuator which would have a certain delay due to standard onboard reducers that usually have a reduction ratio in a range between 100:1 and 500:1. In such a reducer the total delay would be the sum of the delay of each gear multiplied for the reduction rate between them. In this way on onboard actuators the delay can even get to the point of being a

relevant fraction of one motor shaft rotation. Having this kind of play on the chain is the best way to simulate this condition.

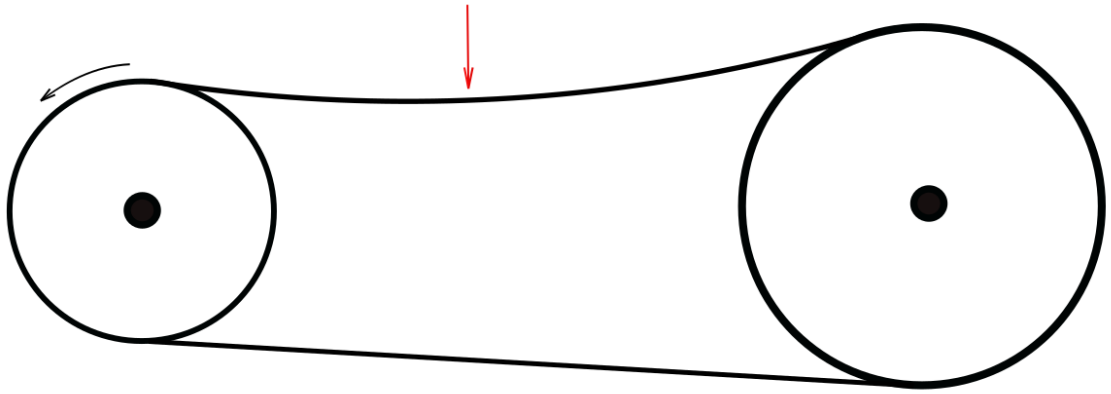

Figure 60: schematization of the side view of a chain-sprocket transmission with highlight on the loose chain

The test bench with respect to the onboard situation will involve smaller loads with smaller reduction rates. In this way, if seen in the right scale, the effects expected on the electric motor present on the bench can be considered really close to the one that would occur on an onboard electric motor in an EMA system. This will of course increase the consistency and reliability of any kind of tests performed on the bench.

The delay introduced in our tests will of course influence the closed loop control law development. Not considering the delay inside the control law would cause instability problems while trying to actuate a position control inside the closed loop.

4 | Future developments and conclusions

This work was developed with the precise intention of laying the foundation for future validations and experimentations in the field of EMAs applications and prognostic algorithms. A complete project is now ready, for the construction of a high fidelity simulator of an EMA and its behaviour during on-board situations. A certain grade of experimentation was planned when the work started but it had to be delayed, due to the unfortunate recent events linked to the COVID 19 virus and the norms applied to preserve the social health. All the work that implied the presence of one or more operator inside a laboratory was postponed. So, right now, many components are still under production or in the assembly phase and in a reasonably close future the test bench is going to be ready to enter the experimental phase to help future works.

In this project it is clearly visible the importance for a system engineer of being able to manage a design approach that, along with the development of a work like this one, can be both internal or from a system point of view.

A systemic approach was required for the design of a coherent and well running "Actuation Module". This process implied giving more emphasis to the interface between each component and to the requirements needed by each one of them to properly function together and accomplish both actuation and data management tasks.

On the other hand, for the design of the "Braking Module", the work had to be approached by designing internally the majority of the components. In parallel with the 3D an 2D design of the components, to ensure the future stability of the global structure, were run several structural tests to see the structure displacement after the application of the weight and the forces implied during a hypothetical simulation. The braking force and braking momentum applied by the disc brake were studied in order to develop the equations necessary to run a Matlab script able to estimate them. Some effort was put in this specific study due to the atypical shape of the braking pad that was a complete circle instead of the classic circular sector shape.

Finally, it is really important to remark that the work on the development and validation of prognostic algorithm that will follow this project, using the simulation system designed in this thesis, is of primary importance in aeronautic sector. Being able to provide data on

when and how a component will fail implies a great advantage from both an economic and a safety point of view.

References

[1] **Qiao G.**, **Liu G.**, **Shi Z.**, **Wang Y.**, **Ma S.**, **Lim T**. *A review of electromechanical actuators for More/all Electric aircrafts systems.* J Mechanical Engineering Science (2018).

[2] **Siemens AG**. *SINAMICS S120 AC Drive Manual.* Nürnberg – Germany (2014).

[3] **Siemens**. *Data Sheet for SIMOTIC S-1FK7. (2020)*

[4] **Riva G.**, *Tesi di laurea magistrale – Development of the test bench of an EMA for prognostic: ideation and realization in additive manufacturing of the conceptual prototype for a reduction gear.* Politecnico di Torino (2019).

[5] **Italsensors.** *Incremental optical encoders.* Online: http://www.italsensor.com/tsw58hs/

[6] **Jacazio G.**, **Piombo B.** *Meccanica Applicata alle Macchine – Vol. II La trasmissione del moto.* Levrotto & Bella (1992).

[7] **Gears.** *Chain Drive Systems.*Online*:* http://gearseds.com/documentation/deb%20holmes/2.5_Chain_drive_systems.pdf